A 3D SPH–FE coupling for FSI problems and its application to tire hydroplaning simulations on rough ground

C. Hermange, G. Oger, Y. Le Chenadec, D. Le Touzé

C. Hermange, G. Oger, Y. Le Chenadec, D. Le Touzé. A 3D SPH–FE coupling for FSI problems and its application to tire hydroplaning simulations on rough ground. Computer Methods in Applied Mechanics and Engineering, 2019, 355, pp.558-590. 10.1016/j.cma.2019.06.033 . hal-02456192

Available online at www.sciencedirect.com

ScienceDirect

Computer Methods in Applied Mechanics and Engineering 00 (2019) 1–32

Comput. Methods in Appl. Mech. and Engrg.

A 3D SPH-FE coupling for FSI problems and its application to tire hydroplaning simulations on rough ground

C. Hermange[a,b], G. Oger[a,*], Y. Le Chenadec[b], D. Le Touzé[a]

[a]École Centrale Nantes, LHEEA res. dept. (ECN and CNRS), Nantes, France
[b]La Manufacture Francaise des Pneumatiques MICHELIN, Clermont-Ferrand, France

---

Abstract

A 3D fluid-structure coupling between Smoothed Particle Hydrodynamics (SPH) and Finite Element (FE) methods is proposed in this paper, with its application to complex tire hydroplaning simulations on rough ground. The purpose of this work is to analyse the SPH-FE coupling capabilities for modelling efficiently such a complex phenomenon. On the fluid side, the SPH method is able to handle the three complex interfaces of the hydroplaning phenomenon: free-surface, ground/fluid and fluid/tire interfaces. On the solid side, the FE method is used for its ability to treat tire-ground contact. A new algorithm dedicated to such SPH-FE coupling strategies is proposed to optimize the computational efficiency through the use of differed time steps between fluid and solid solvers. This way, the number of calls to the FE solver is minimized while maintaining the accuracy and stability of the coupling. The ratio between these respective time steps relies on a control procedure based on pressure loading. The present 3D SPH-FE model is first validated with different academic test cases and experimental data before considering the complex problem of the 3D hydroplaning simulations. Hydroplaning simulations are performed and analyzed on 3D configurations involving both smooth and rough grounds.

Keywords: SPH-FE Coupling, Fluid-structure interactions, Tire hydroplaning

---

1. Introduction

Hydroplaning phenomenon is well known for all drivers. This phenomenon stands as a challenging problem both for tire and car industries. It strongly influences the tire grip properties on wet roads, especially for road braking and turning. It corresponds actually to a loss of the contact surface between the tire and the road. A part of the water is evacuated through the grooves while the other one is discharged in front of the tire, imposing a strong pressure on the tread. When a critical velocity is reached, vertical fluid forces become too large to maintain the contact between the tire and the road, affecting the available tire/road forces. A better understanding of the hydroplaning generating mechanisms is therefore needed to design safer tires. The use of numerical tools is needed to answer this issue, in view of predicting tire performances and complementing the difficult and expensive experimental tests. Simulations can provide additional information which are still unavailable through experiments, while experiments are still critical for validation purposes.

---

[*] Corresponding author
Email address: `guillaume.oger@ec-nantes.fr` (G. Oger)

The hydroplaning phenomenon such as many violent FSI problems involve some non-negligible coupling effects due to the presence of strong reciprocal interactions. The growth of computational power has enabled their modelling, resulting in the development of various numerical methods to model these coupled phenomena. In the last decades, mesh-based methods were preferred on this topic. The Finite Element (FE) method is classically used for structure modelling [7], while several methods can be used for fluid modelling such as Finite Volume (FV), Finite Difference (FD) or FE methods. The hydroplaning problem has been the topic of simulation works since the 90's [30] emphasizing its complexity (see [15, 64, 39]): fluid-structure interactions (FSI), highly deformable body, structure modelling with complex materials involved, contact with asphalt and the complexity of the resulting fluid flow (extremely complex interface, road dry up, ventilation, possible development of turbulence and cavitation). All these aspects lead to challenging problems for the numerical simulations of both fluid and solid domains. Most of the literature related to the hydroplaning problem is focused on the use of mesh-based methods using FD-FE ([57, 37]), FE-FE ([38]) and FV-FE coupling strategies ([58, 52]). Each of these methods possess its own specifications concerning the viscous model, the compressible fluid, etc. The presented hydroplaning configurations of these works considered high water height values, from 4 to 10 mm. It seems that these models have some difficulties to consider smaller heights. Nevertheless the current regulatory wet braking tests imposed by the European regulation N2009/1222 deals with water depth about 1 mm above the average roughness of the road. It also appears that these mesh-based approaches have some difficulties to deal with the different complex interfaces of the phenomenon: the free-surface and the fluid-structure interfaces. Especially large deformations of the fluid domain lead to the need for re-meshing tools and expensive computational costs [3].

Furthermore, classical hydroplaning simulations [15, 64, 5] considered a smooth ground. Nevertheless, the actual road is not smooth but conversely presents large irregularities. The slope of the road, its structure and surface roughness all contribute to water dispersal. However, these factors do not disperse all the water. When the road is wet, water may creep in between the rubber and the road. The deeper the water and the greater the vehicle speed, the more this effect is amplified, eventually impairing grip potential. Some studies focused on vehicle hydroplaning on grooved pavements [3]. However, these studies were still far from considering a real rough ground. Zhu *et al.* [70] and Li *et al.* [43] proposed aquaplaning simulations using a realistic rough ground within demonstrative test cases. The use of meshless method such as for instance SPH [45, 27] or Moving Particle Semi-Implicit (MPS) [28] for the fluid resolution is particularly meaningful. A mesh-based method would not be able to dry the road, especially considering rough roads. The meshfree methods seem therefore perfectly adapted to introduce macro-roughness into the model and to capture additional phenomena related to the combined presence of water and roughness (draining mechanisms and fluid confinement inside the roughness of the ground for instance). Note that the dynamic treatment of the contact between the tire and a dry rough ground is already a great challenge for the FE method. In this context, the interest of the SPH method for modelling efficiently the hydroplaning flow has been demonstrated by Barcarolo *et al.* [5] using a rigid body assumption, and more recently with fluid-structure interactions by El Gindy and El Sayegh [22] and Qu *et al.* [60]. These last studies use smooth grounds in their simulation. The meshless methods naturally avoid the problem of fluid/solid grid compatibility. The other significant advantage of these methods, in this context, consists in its ability to be coupled with conventional FE solvers[25, 36, 68] as well as with particle-based solvers for the structure [35, 32, 21, 2].

In this work, a partitioned coupling approach has been retained with the formalism introduced by Fourey *et al.* [25]. This paper focuses on hydroplaning simulations through the combination of a Lagrangian particle method and a classical meshed structure method as an extension of our previous works [25, 31]. The solid part is modelled with a classical FE method. On the fluid side, the SPH method can efficiently handle the three complex interfaces present in the hydroplaning phenomenon: the free-surface, the ground/fluid and the fluid/tire interfaces. It is perfectly suitable for such simulations involving large deformations in both fluid and solid sub-domains.

Various SPH-FE coupling methods have already been proposed since the 90's (see Johnson [34] and Attaway *et al.* [4]). The majority of the strategies are based on a master-slave coupling, in which contact forces are computed to prevent the penetration of SPH particles into the FE meshes. Each method proposed has its own specificity. For instance, De Vuyst *et al.* [18] considered the FE nodes as SPH particles. Groenenboom and Cartwright [29] used a master-slave scheme to compute a penalty force to prevent interface penetration and to satisfy the momentum conservation. Furthermore, SPH-FE coupling can be used for FSI or solid impact problems [69, 11]. Nevertheless, no contact algorithm dedicated to avoid material interpenetration is needed. No special treatment is prescribed for the deformable body interface, as demonstrated by Fourey *et al.* [24, 25] and by Yang [66]. They showed the interest of SPH-FE coupling for complex FSI problem modelling without contact algorithms for free-surface flows using elastic structures. Both validated their coupling strategy on several 2D FSI benchmarks with increasing complexity. They showed the capability of such implementation to be easily coupled with different software. Nevertheless, in their work on coupling algorithms Michler *et al.* and Degroote *et al.* [50, 19] underlined that partitioned algorithms do not permit the exact satisfaction of interface conditions, contrary to monolithic schemes. Therefore Fourey *et al.* [25] analysed the SPH-FE coupling robustness according to various coupling parameters, highlighting the need for a sufficient dissipation on the high frequency domain to maintain stable calculations. This coupling strategy has also been validated through an energetic point of view by Hermange *et al.* [31] ensuring the validity of such an approach. Furthermore Li *et al.* [41, 43] proposed a SPH-FE coupling strategy (then improved by Nunez *et al.* [53]) ensuring energy conservation through the fluid-structure interface. Nevertheless the latter technique is strongly intricated with the FE model, and therefore implies hard-coding within the solid solver. It seems therefore more costly and less flexible. Thereby the formalism developed in 2D by Fourey *et al.* [25] and Hermange *et al.* [31] has been retained in this study. These previous works issue to a weak-coupling strategy which is flexible, easy to implement and compatible with any kind of SPH schemes and boundary condition treatment [25]. No additional CPU time is introduced as no interface treatment is required. The overall energy conservation is satisfied by the use of fine spatial resolutions [31]. In this work, an extension of this approach to a 3D model is performed. The efficiency of such simulations is also considered by proposing a new algorithm dedicated to SPH-FE coupling strategy and its application to the hydroplaning phenomenon.

The present paper is organized as follows: Section 2 introduces the SPH model. Section 3 presents the SPH-FE coupling strategy. Section 4 investigates a validation of the 3D FSI strategy on different experimental test cases. Section 5 is dedicated to present the tire hydroplaning simulation model. Finally, numerical results are presented and discussed in Section 6.

2. SPH model

A weakly-compressible and inviscid fluid is considered in this paper. Navier-Stokes equations are therefore reduced to the following Euler equations (written in a moving Lagrangian referential):

$$\frac{d\vec{x}}{dt} = \vec{v}, \tag{1}$$

$$\frac{d\rho}{dt} = -\rho\vec{\nabla}.\vec{v}, \tag{2}$$

$$\frac{d\vec{v}}{dt} = \vec{g} - \frac{\vec{\nabla}P}{\rho}, \tag{3}$$

where $\vec{x}$, $\vec{v}$, ρ and P are respectively the position, velocity, density and pressure. This system is closed using the following equation of state:

$$P = \frac{\rho_0 C_0^2}{7}\left[\left(\frac{\rho}{\rho_0}\right)^7 - 1\right], \tag{4}$$

where ρ_0 and C_0 are respectively the reference density and speed of sound.

In the SPH formalism, the space differential operators in the above system are approximated using a convolution based on a kernel function W [27]. Here the Wendland kernel [65] function is used. The fluid field is described by a set of particles (elementary fluid volumes), carrying the discrete field values within the fluid domain. The simulations discussed in this paper are performed using a Riemann-SPH scheme [63]. In the present work, we preferred a variant of this formulation proposed by Leduc *et al.* [40], where the local mass conservation is ensured. It implies a purely Lagrangian description of the medium. The scheme considered here is defined by the following system:

$$\frac{d\vec{x}_i}{dt} = \vec{v}_i, \tag{5}$$

$$\frac{d\omega_i}{dt} = \omega_i \sum_{j=1}^{N} 2(\vec{v}_e - \vec{v}_i).\vec{\nabla}_i W_{ij}\omega_j, \tag{6}$$

$$\frac{dm_i}{dt} = 0, \tag{7}$$

$$\frac{dm_i\vec{v}_i}{dt} = \omega_i\rho_i\vec{g} - \sum_{j=1}^{N} 2P_e\vec{\nabla}_i W_{ij}\omega_j\omega_i, \tag{8}$$

where P_e and $\vec{v}_e$ are the linearized Riemann problem solutions at interface $i-j$, and $\rho_i, \omega_i, \vec{x}_i, \vec{v}_i$ are respectively the density, volume, position and velocity of the particle i. N represents the number of fluid particles inside the kernel support.

The time advance is performed explicitly using a 4^{th} Runge-Kutta scheme, with the following CFL condition on time steps:

$$\Delta t < CFL\frac{R}{C_o}, \tag{9}$$

where R is the kernel radius and CFL is the Courant number taken as $CFL = 0.375$. This feature leads classically to very small time steps. Theoretically a double convergence condition is required in the method SPH method (see for instance Quinlan *et al.* [61] or Oger *et al.* [54]). The first one addresses the main spatial resolution parameter, and refers directly to the measure of the kernel-based approximation, that is:

$$R \to 0, \tag{10}$$

while the second one refers to the quadrature of the convolution integral, as:

$$\frac{R}{\Delta x} \to \infty, \tag{11}$$

where Δx is the characteristic distance between two particles. Note that this latter condition cannot be satisfied in practice. Instead, the values commonly adopted in the literature for $\frac{R}{\Delta x}$ are in the range $2 < \frac{R}{\Delta x} < 4$, which corresponds to 20 to 60 neighbors in 2D. With such a high number of neighbors, the residual error on the second convergence criterion is sufficiently low in practice for permitting to reach acceptable convergence saturation errors. For cases involving violent fluid-structure interaction problems, we usually expect the fluid time step to remain smaller than the solid one.

Effects of structure deformations onto the fluid are imposed through the boundary conditions exclusively which are therefore a key point in the present coupling strategy. Boundary conditions are imposed through the use of ghost particles [44, 16] or the Normal Flux Method (NFM) [47, 46, 17].

Ghost particle method The ghost particles are used to complete the kernel support of a particle located near a boundary, in order to enforce the kinematic and dynamic boundary conditions. Theoretically, the ghost particle pressure should take into account the local body acceleration [10, 49]:

$$\frac{\partial P}{\partial n} = \rho\left(\frac{d\vec{V}_{wall}}{dt}.\vec{n} - \vec{g}.\vec{n} + (\vec{V}_{wall} - \vec{V}).\frac{dn}{dt}\right), \tag{12}$$

where $\vec{n}$ and $\vec{V}_{wall}$ are respectively the local normal and the velocity. Nevertheless for the applications considered in this work, we suppose that the contributions $\frac{d\vec{V}_{wall}}{dt}.\vec{n}$ and $(\vec{V}_{wall} - \vec{V})\frac{dn}{dt}$ are negligible compared to other components. As a result, the ghost particle pressure $P_{G(i)}$ and velocity $\vec{v}_{G(i)}$ are defined as:

$$P_{G(i)} = P_i - \rho_i(\vec{g}_i.\vec{n})\left[(\vec{x}_i - \vec{x}_{G(i)}).\vec{n}\right], \tag{13}$$

$$\vec{v}_{G(i)} = \vec{v}_i + 2(\vec{V}_{wall}.\vec{n} - \vec{V}_i.\vec{n})\vec{n}. \tag{14}$$

Normal flux method For complex geometries, the creation of ghost particles is not straightforward and results in a possibly large algorithmic complexity. The Normal Flux Method (NFM) can be used to overcome this limitation. As illustrated in Fig. 1, in this technique the kernel support of the particle is not completed. Instead the Normal Flux Method introduces the calculation of the surfacic term in the SPH gradient approximation:

$$< \vec{\nabla}_{\vec{x}}\phi(\vec{x}) >= \int_D \phi(\vec{y})\vec{\nabla}_{\vec{x}}W(\vec{x}-\vec{y})dV_{\vec{y}} + \int_{\partial D} \phi(\vec{y})W(\vec{x}-\vec{y})\vec{n}dS_{\vec{y}}. \tag{15}$$

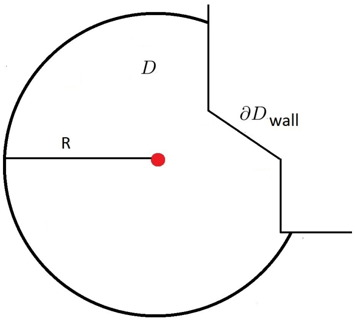

Figure 1. Normal flux method.

The main advantage of this method is a better handling of complex geometries. We refer the reader to [13, 47, 46, 17] for more details. The formalism presented in De Leffe [17] and Chiron *et al.* [13] is adopted in the present work.

3. SPH-FE coupling strategy

The same SPH-FE coupling strategy as Fourey *et al.* [25] is considered here, which is based on classical partitioned approaches. Here the deformable body behaviour is modelled using the commercial software: *Abaqus* (developed by *Simulia*). The fluid part is modelled using *SPH-flow*, jointly developed by *Ecole Centrale Nantes* and *NEXTFLOW Software* [55, 56].

3.1. Coupling algorithm

According to Fourey *et al.* [25], a *Conventional Parallel Staggered* (CPS [23]) procedure is considered here. The time step is the same for both fluid and solid solvers. As the maximum fluid time step allowed is expected to be smaller than the solid one, *SPH-flow* imposes its time steps to the FE solver. This condition is always satisfied using an explicit resolution in the fluid and an implicit one in the solid. In practice the fluid solver sends its time step value and pressure loads to the FE solver and receives the body node positions and velocities. Then both solvers simultaneously evolve from instant t^n to t^{n+1} (see Fig. 2). The calculation time of fluid and solid solvers are overlapped by a synchronous processing.

This CPS algorithm makes the assumptions that the fluid loading $F_{fluid/body}$ does not vary significantly between instants t^n and t^{n+1} (i.e. $F^{n+1}_{fluid/body} \approx F^{n}_{fluid/body}$), which is acceptable since the weakly compressible approach imposes very small time steps. Note that no sub-iterations are performed to ensure velocity and pressure agreements at the fluid/solid interface. There is no convergence or stability control during the simulation, which differs from common practice adopted with conventional mesh-based methods. Thus, it introduces a “natural” convergence in time which helps in stabilizing the coupling.

Depending on the physics of the FSI problem, one of the two sub-domains needs smaller time steps. For the present SPH-FE coupling, time steps are expected to be smaller within the fluid domain: the CFL condition imposes small fluid time steps due to the fine spatial resolution. Furthermore, computational times are larger in the serial FE solver given the parallel nature of SPH-flow [55]. Contact interactions between the tire and the road also require fine solid spatial resolutions, inducing large CPU times for the FE simulation. Consequently, CPU times are mostly ruled by the solid part.

This paper proposes an optimization consisting in authorizing several fluid time steps within each solid one. Recently Nunez *et al.* [53] proposed such a coupling strategy able to integrate each domain with different time steps by adapting the energy-conserving procedure proposed by Li *et al.* [43]. However a partitioned approach is still considered in this work. As a consequence the CPS procedure used by Hermange *et al.* [31] and Fourey *et al.* [25] should be adapted. Here we propose to introduce a ratio p between fluid and solid time steps (see Fig. 3). A linear extrapolation of the structure coordinates is carried out for each fluid time step according to:

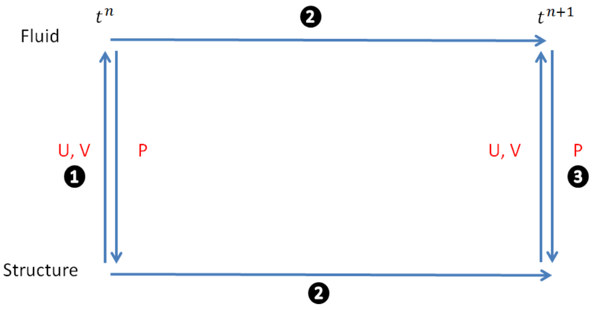

Figure 2. **CPS** coupling algorithm.

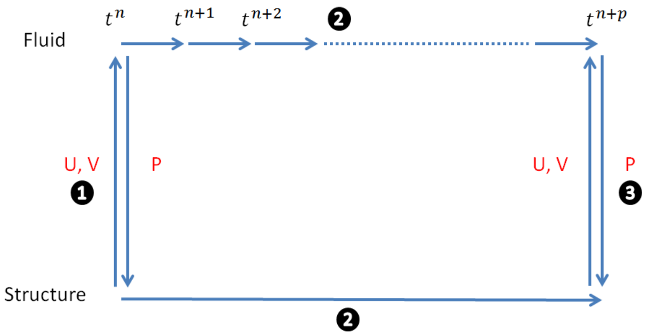

Figure 3. **CPS** Coupling algorithm with a time step ratio p between each sub-domain.

$$\vec{x}_i^{n+l} = \vec{x}_i^n + l\Delta t\vec{v}_i^n, \quad \text{for } l = 1, ..., p \tag{16}$$

where $\vec{x}_i$ and $\vec{v}_i$ are the positions and velocities of the node i.

In addition, a regulation of the ratio p is performed according to the variations of the fluid loads at the end of each loop as:

$$\begin{cases} p = p-1 & \text{if} \quad 0.075 < \dfrac{\left|\sum_k \left\|\vec{F}^{k,n+p}_{fluid/body}\right\| - \sum_k \left\|\vec{F}^{k,n}_{fluid/body}\right\|\right|}{\sum_k \left\|\vec{F}^{k,n}_{fluid/body}\right\|} \leq 0.15 \text{ and } p \geq 2 \\ p = p+1 & \text{if} \quad \dfrac{\left|\sum_k \left\|\vec{F}^{k,n+p}_{fluid/body}\right\| - \sum_k \left\|\vec{F}^{k,n}_{fluid/body}\right\|\right|}{\sum_k \left\|\vec{F}^{k,n}_{fluid/body}\right\|} \leq 0.075 \\ p = 1 & \text{otherwise} \end{cases}, \tag{17}$$

where $\vec{F}^{k,n}_{fluid/body}$ is the fluid loads on the wet FE face k at instant t^n. Indeed, numerical experiments showed that the assumption $F^{n+p}_{fluid/body} \approx F^n_{fluid/body}$ is no longer ensured when the force variations between two successive loops reach 7.5%. This procedure allows to increase the number of fluid-structure interactions when needed, and to correctly capture all coupling effects. Furthermore if a variation exceeds 15%, the ratio p is directly reduced to 1 in order to maintain the validity of the solution during violent fluid impacts on deformable structures characterized by abrupt impact pressures. Otherwise the ratio p is increased by one, within a limit defined at the beginning of the simulation.

Furthermore, each loop should ensure:

$$\Delta t^{FE} = p\Delta t^{SPH}, \tag{18}$$

Note that defining the SPH time step size beforehand (Δt^{n+1}, Δt^{n+2},...) is theoretically impossible since the CFL condition involves the sound speed which varies at each instant, based on the particle densities. A prior estimation of the time step is therefore used, by choosing Δt^n imposed by the CFL condition (9) and by limiting its size for safety purpose as:

$$\Delta t^{n+i} = 0.8\Delta t^n, \quad \forall i = 1, ..., p \tag{19}$$

$$\Delta t^{FE} = 0.8p\Delta t^n. \tag{20}$$

Note that it is necessary to preserve a solid time step in agreement with the physics (structural vibrations, etc.). Concerning the computational costs, the speedup S_p of this new algorithm is defined as:

$$S_p = \frac{CPU^{\text{without p ratio}}}{CPU^{\text{with p ratio}}}. \tag{21}$$

Calling t^{FE} and t^{SPH} the CPU times per time step respectively for the FE and SPH solvers, the speedup can be expressed as:

$$\begin{cases} S_p = \frac{pt^{FE}}{\frac{1}{0.8}t^{FE}} = 0.8p & \text{if} \quad t^{FE} > pt^{SPH} \\ S_p = \frac{t^{FE}}{\frac{1}{0.8}t^{SPH}} & \text{otherwise} \end{cases}. \tag{22}$$

Practically, both SPH and FE solvers are considered as black boxes exchanging fluid pressure loads and structure node positions and velocities with a dedicated third program (coupling program) responsible for managing the data exchanges needed (MPI communications), so that any SPH or FE software can actually be used (Fig. 4).

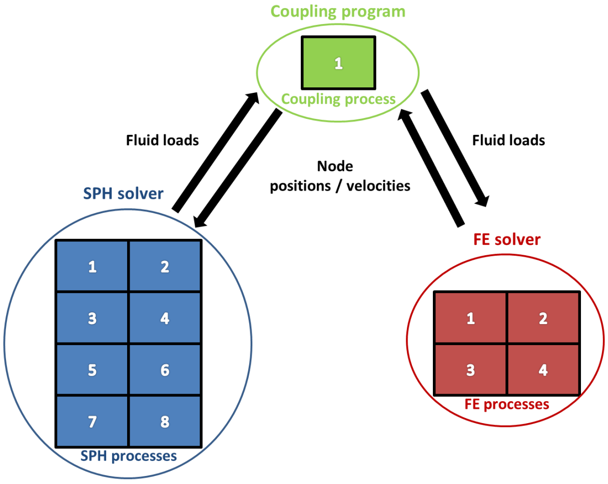

Figure 4. SPH-FE coupling strategy. Example involving 8 cores and 4 cores respectively for SPH and FE solvers. A single core is dedicated to the coupling program.

3.2. Fluid loads on the deformable structure

From the SPH algorithmic point of view, a deformable body at instant t is considered as a rigid wall, but with specific local deformation velocities (and node displacements) provided by the FE solver. It is possible to choose any boundary conditions, ghost particle method or NFM. No other treatment is prescribed to treat the deformable body interface. On the other hand, no contact algorithm dedicated to avoid material interpenetration is needed, contrary to Groenenboom and Cartwright [29] for instance. The pressure loads P_k applied to the FE face k is computed using reciprocal forces between fluid and solid media. When using the ghost particle method, this is achieved through the summation of ghost particle interactions with fluid particles, as proposed for instance by Bouscasse *et al.* [10] and Marrone *et al.*[48] for rigid bodies. The force can be expressed as:

$$\vec{F}_{fluid/body} = -\vec{F}_{body/fluid} = -\sum_{i=1}^{N_{FP}}\sum_{j=1}^{N_g}[-2P_E]\vec{\nabla}_i W_{ij}\omega_i\omega_j, \tag{23}$$

where N_g is the number of ghost particles

Obviously in the case of a deformable body this force should be decomposed on each panel k, so that:

$$\vec{F}_{fluid/body} = \sum_{k=1}^{N_p}\vec{F}^k_{fluid/body}, \tag{24}$$

with

$$\vec{F}^k_{fluid/body} = \sum_{i=1}^{N_k}\sum_{j=1}^{N_g}[-2P_E]\vec{\nabla}_i W_{ij}\omega_i\omega_j, \tag{25}$$

where N_P is the number of panels and N_k is the set of particles seen by the wet panel k (see Fig. 5). As the calculation of ghost interactions is needed anyway for imposing boundary conditions, pressure forces $\vec{F}^k_{fluid/body}$ are transferred to the FE solver at the end of each first Runge-Kutta stage. Using NFM, the principle is the same but using the summation of panel interactions with fluid particles.

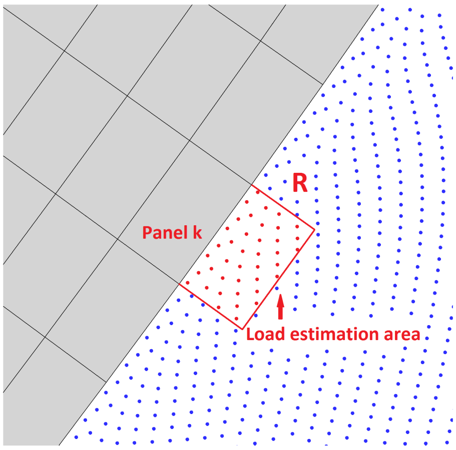

Figure 5. The set of particles seen by the body panel k.

4. 3D validation of the SPH-FE coupling strategy

It seems important to investigate the relevance of our 3D SPH-FE model on validation test cases before considering the complex problems of 3D hydroplaning.

4.1. Dam-break flow through an elastic gate

Here, we propose to validate the present coupling onto a dam-break flow through an elastic gate. The fluid initially at rest is contained within a rigid tank closed using an elastic gate, located on the left side. At $t = 0$ s the elastic gate is released to let the water escape. This test case has been first introduced by Antoci [1], according to the configuration presented in Fig. 6 and Tab. 1. In their study, Antoci *et al.* [2] used a monolithic approach with a SPH-SPH coupling to model this FSI problem and proposed some comparisons with their own experimental data. Here 3D and 2D simulations are performed and the results are compared to the experimental data from Antoci *et al.* [2] and the 2D numerical results from Li *et al.* [42].

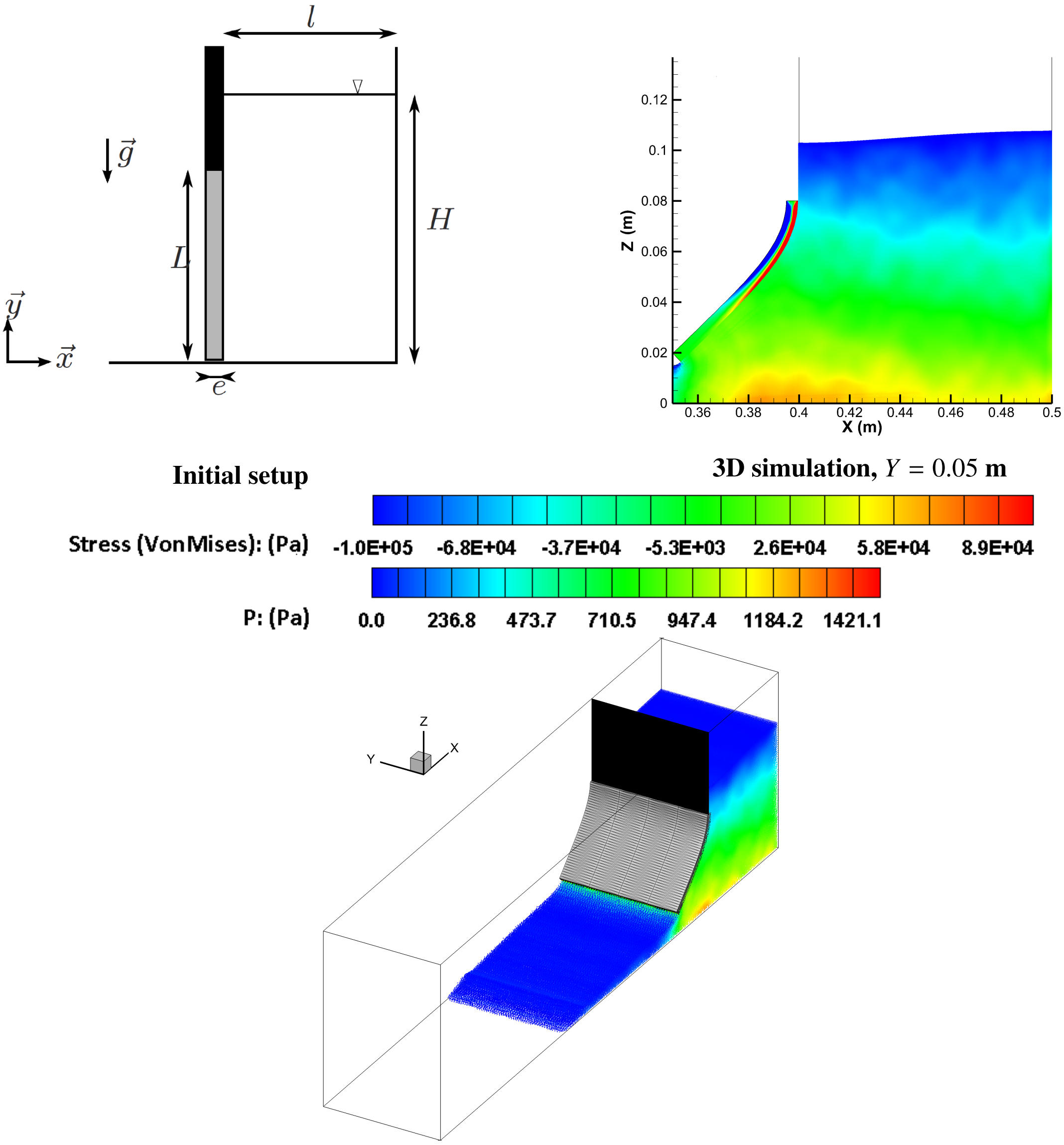

Figure 6. Antoci *et al.* snapshot at t = 0.16 *s* of the present 3D simulation.

The particles are distributed uniformly in the fluid medium. The FE mesh is composed of 4 width-wise, 4 depth-wise and 40 length-wise elements. The rubber behaviour is still considered as incompressible with a Poisson coefficient close to 0.5. The non-linear deformation law presented in Fig. 7 is used to model the rubber gate behaviour. The boundary conditions are imposed using the ghost particle method [16]. Furthermore, the CPS procedure with $p = 2$ and $R/\Delta x_{SPH}$ values are retained as the best compromise among accuracy, stability and computational time.

L	$79\ mm$
H	$0.14\ m$
e	$5\ mm$
l	$0.1\ m$
ρ_{rubber}	$1100\ kg.m^{-3}$
ρ_{water}	$1000\ kg.m^{-3}$
g	$9.81 m.s^{-2}$

Δx_{FE}	$1.25\ mm$
Δy_{FE}	$25\ mm$
Δz_{FE}	$1.975\ mm$
Δx_{SPH}	$1\ mm$
$R/\Delta x_{SPH}$ (3D)	2.11
$R/\Delta x_{SPH}$ (2D)	4.0
C_0	$25.0\ ms^{-1}$
CFL number	0.375

Table 1. Physical and numerical parameters for the dam-break through an elastic gate.

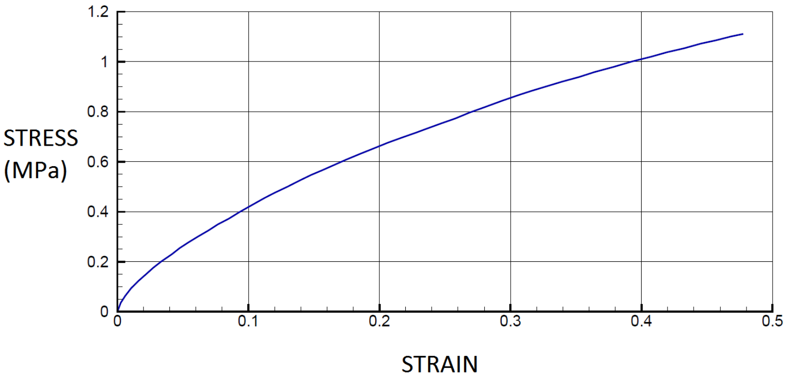

Figure 7. Strain-stress curve related to the rubber used in the simulations.

Fig. 8 compares the experimental and numerical time histories of the gate tip displacement. Numerical results are in good agreement with the experiments from [2]. The global trend of the gate deformation is captured. The abrupt decrease of the displacement observed experimentally from instant $t = 0.32$ s is not reproduced by our coupling. No leakage of fluid is observable in the simulation (contrary to the experiment). This was expected since a free slip condition is considered between the gate and the tank. Furthermore, the 3D numerical results are in good agreement with the 2D ones and with the 2D numerical model of Li *et al.* [43].

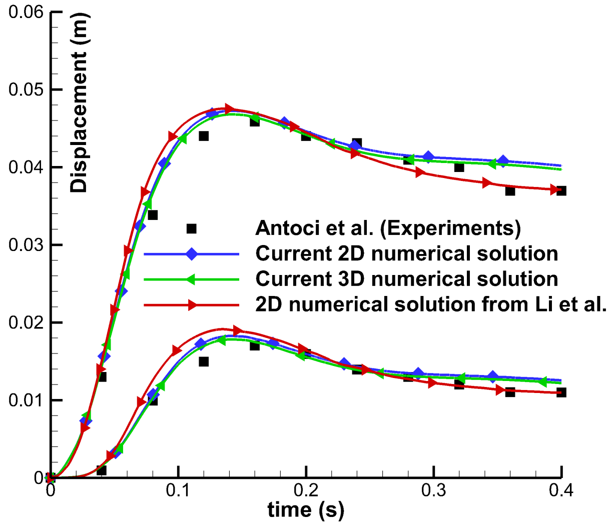

Figure 8. Time history of the horizontal (top) and vertical (bottom) displacements of the gate tip for different FSI models compared to experiments.

Fig. 9 compares the experimental and numerical water height time histories behind the gate (x = 0.4 m) and at x = 0.45 m. Good agreements are observed despite a small underestimation of the water level. Exactly as for the 2D results, it seems that the present results show a small persisting offset of about 0.04 s. The origin of this difference is not clearly identified, but may be imputed to experimental uncertainties, since the experimental water level tends (surprisingly) to remain stable in the first instants while the gate starts to deform.

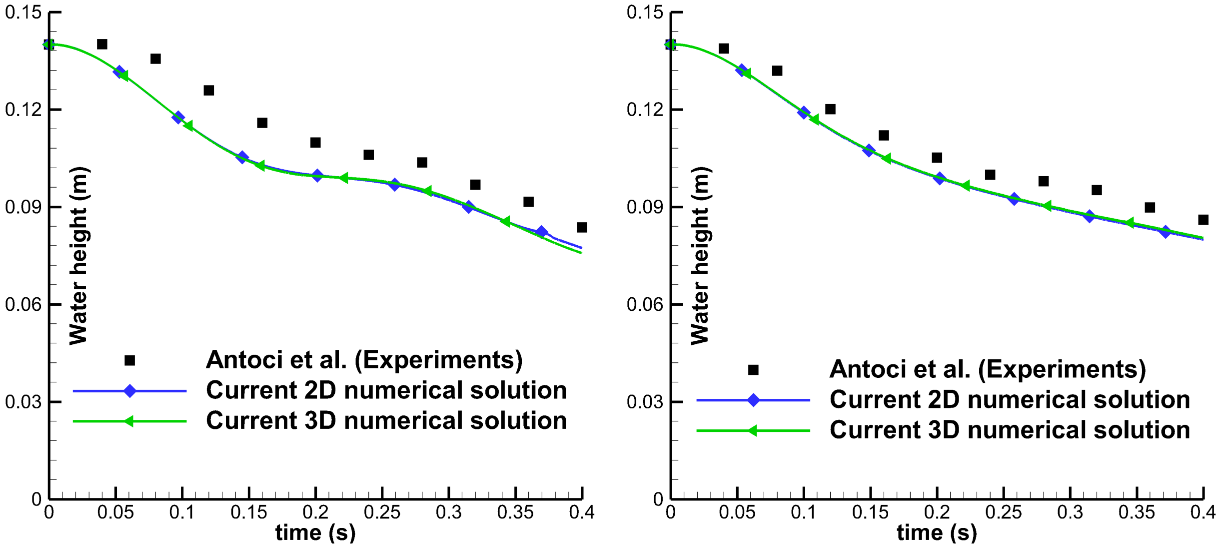

Figure 9. Water height evolutions at locations x = 0.4 m (left) and x = 0.45 m (right) obtained with the present FSI model compared to experiments.

Fig. 10 shows the fluid pressure field at various instants for the 2D and 3D models, and experimental snapshots are also provided. Except the leakage of water between the gate and the wall that is present in the experiments, the FSI interactions seem correctly reproduced by both the present 2D and 3D models. Nevertheless, additional experimental data would still be needed. For instance, PIV measurements would be useful to validate the numerical velocity field.

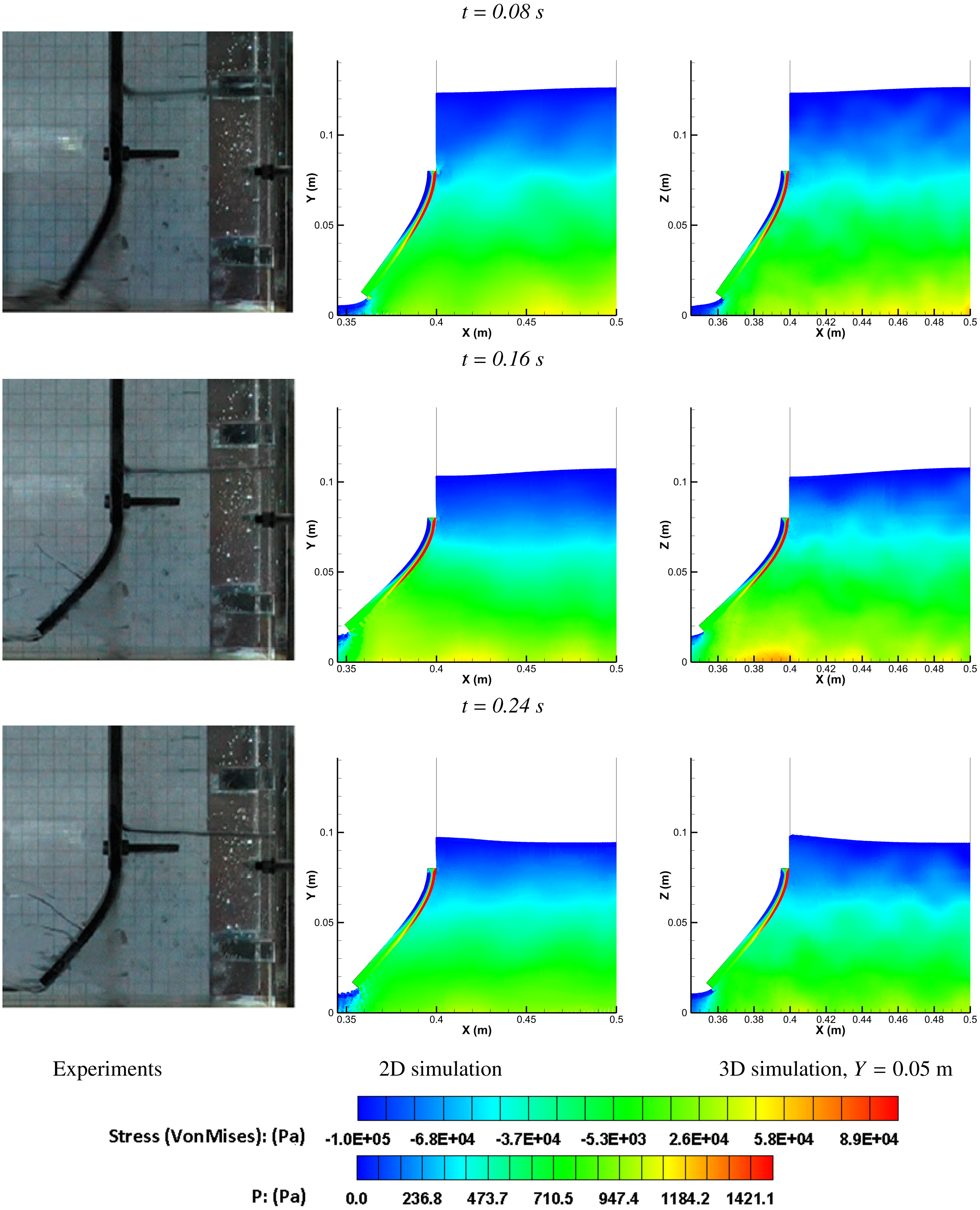

Figure 10. Fluid pressure field at different instants (rows) for different FSI models compared to corresponding experimental snapshots from Antoci *et al.* experiments [2].

4.2. *Sloshing tank interactions with an elastic beam*

The second validation cases consists in a sloshing tank interacting with a deformable clamped beam. This test case has been introduced by Idelsohn *et al.* [33] and described in [9]. The two initial configurations tested are provided in Fig. 11. A rectangular tank containing a clamped beam is filled with sunflower oil (two different levels). A forced roll motion is then applied to the tank (as shown in Fig. 12) with the center of rotation located at the midpoint of the tank bottom. Furthermore, the period is chosen so as to coincide with the critical sloshing frequencies, according to the filling level. The deformable beam is clamped at the bottom of the tank (origin)

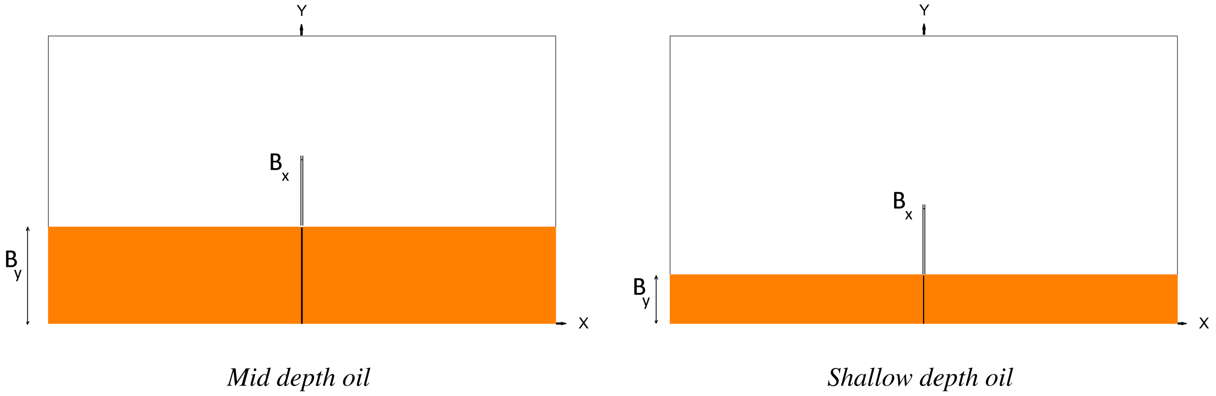

Mid depth oil *Shallow depth oil*

Figure 11. Two initial configurations of the FSI sloshing problem with elastic beams [9].

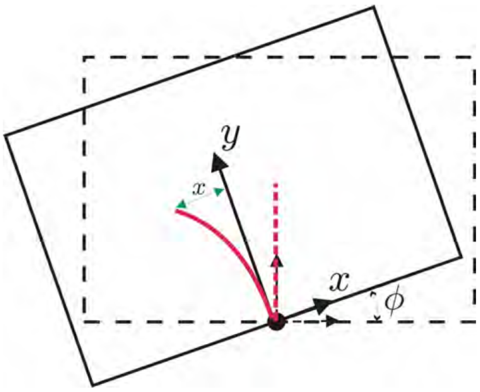

Figure 12. Sloshing tank interactions with an elastic beam: rolling tank configuration [9].

Two blowholes are located at the top of the tank to let the air circulate freely. The air phase can therefore be legitimately omitted provided that no air entrapment occurs. The particle refinement technique proposed by Barcarolo *et al.* [6] and improved by Chiron *et al.* [12, 14] is used to limit the total number of fluid particles involved. The viscous nature of the flow is modelled using the Monaghan & Gingold formulation expressed in [51].

The FE mesh is composed of 8 width-wise, 8 depth-wise and 80 length-wise elements. The beam material is a commercial neoprene rubber. For which no experimental strain-stress curve is available. The rubber behaviour is considered as incompressible with a Poisson coefficient close to 0.5 and the beam deformation is modelled by a linear elastic law, with $E = 6$ MPa. In each case, a gap of 2.9 mm exists between the clamped beam and the tank in the transverse $\vec{z}$ direction (see Fig. 13). Finally, the boundary conditions are imposed using the ghost particle method [16].

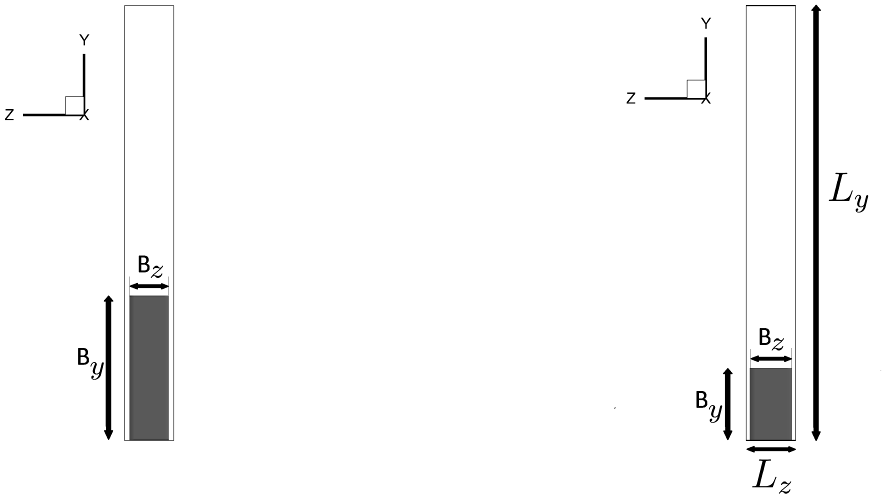

Mid depth oil

Shallow depth oil

Figure 13. Sloshing tank interactions with an elastic beam: gaps between the clamped beam and the tank in the transverse direction ($\vec{z}$ direction) [9].

4.2.1. Clamped beam in mid depth oil configuration

The mid depth configuration corresponds to a 114.8 mm oil depth. This test case has already been studied in 2D by Yang *et al.* [67] and in 3D by Gilbert [26]. Nevertheless, the flow concerns a viscous fluid in a narrow tank. The effects of the no-slip condition on the lateral walls cannot be neglected. Consequently, the use of a 3D model is crucial here. The particle refinement technique is used to limit the total number of particles involved according to the configuration presented in Fig. 14. Three refinement levels are considered, where $\Delta x_{SPH} = 4$ mm in the coarsest zone. All simulation parameters are presented in Tab. 2. $R/\Delta x_{SPH}$ is chosen equal to 2.11 for computational purpose.

Tank dimensions	$L_x = 609\ mm$ $L_y = 334.5\ mm$ $L_z = 39\ mm$
Beam dimensions	$B_x = 4\ mm$ $B_y = 114.8\ mm$ $B_z = 33.2\ mm$
Oil depth	$114.8\ mm$
Poisson coefficient ν	≈ 0.5
Young Modulus	$6\ MPa$
ρ_{rubber}	$1100\ kg.m^{-3}$
ρ_{oil}	$917\ kg.m^{-3}$
ν_{oil}	$5.10{-}5\ m^2.s^{-1}$
g	$9.81\ m.s^{-2}$

Δx_{FE}	$0.5\ mm$
Δy_{FE}	$1.435\ mm$
Δz_{FE}	$4.15\ mm$
Δx_{SPH}	$1\ mm$
$R/\Delta x_{SPH}$	2.11
C_0	$15.0\ m.s^{-1}$
CFL number	0.375

Table 2. Physical and numerical parameters for the sloshing tank interactions with an elastic beam in mid-depth oil.

In this case, the amplitude of the roll motion is about 4 degrees (Fig. 15). The clamped beam therefore presents large deformation amplitudes. Fig. 16 shows the time history of the local x-displacement (as shown in Fig. 12) of the beam extremity. The present numerical results are in good agreements with the experimental data from Boita-Vera [9] and the numerical results from the literature, both in phase and in amplitude.

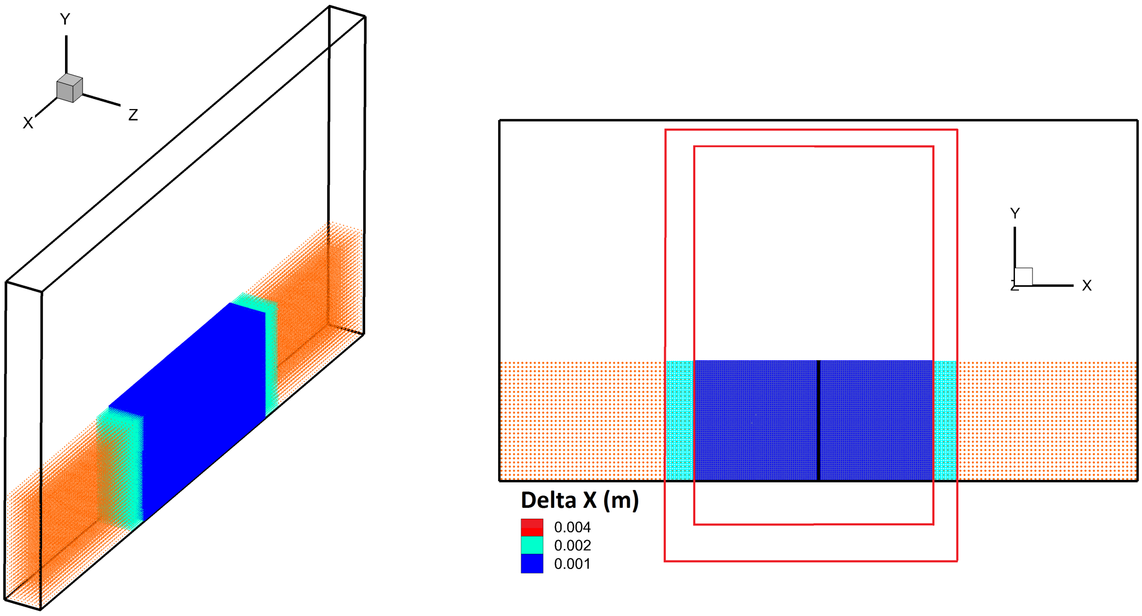

Figure 14. Sloshing tank interactions with a clamped beam in mid depth oil with two refinement boxes (red) [9].

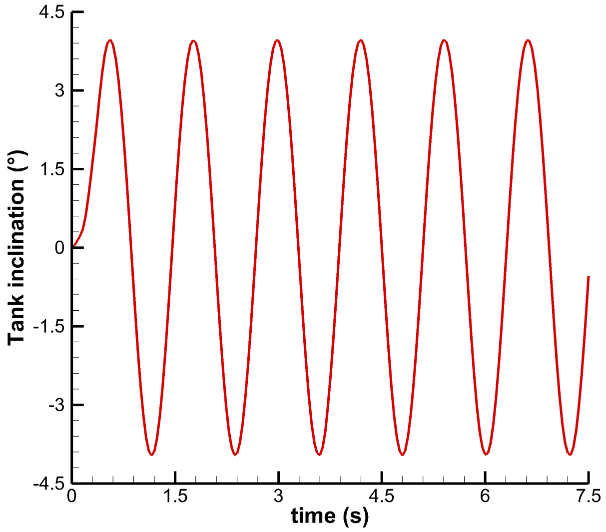

Figure 15. Time history of the forced roll motion for the sloshing tank interactions with an elastic beam in mid-depth oil.

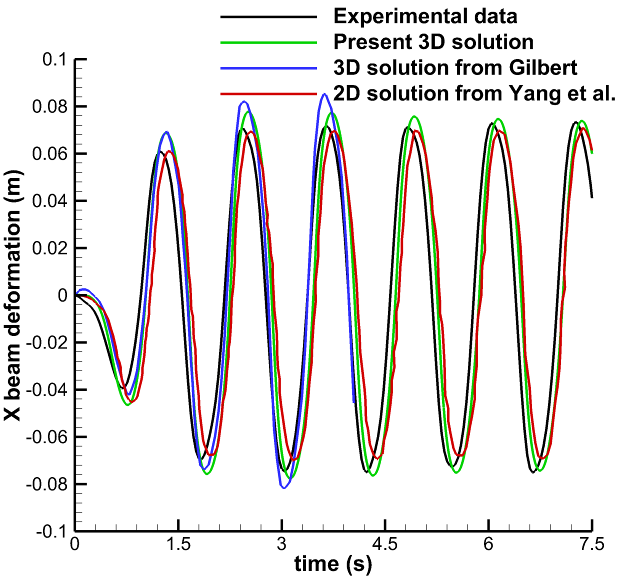

Figure 16. Time history of the local x-displacement of the beam extremity for the sloshing tank interactions with an elastic beam in mid-depth oil.

Fig. 17 displays the fluid pressure field and compares the present results to the experiments at different instants. A good agreement is observed for the free surface deformations. This problem seems correctly predicted by the proposed SPH-FE coupling. However, complementary data would be needed detailed for a more validation of the numerical model, such as PIV measurements for the velocity field and local pressure probes. The use of a 3D model is crucial here. The fluid flow is much more dynamic in 2D simulations since the viscous effects on the lateral walls are not considered (see Fig. 18).

t = *1.84 s*

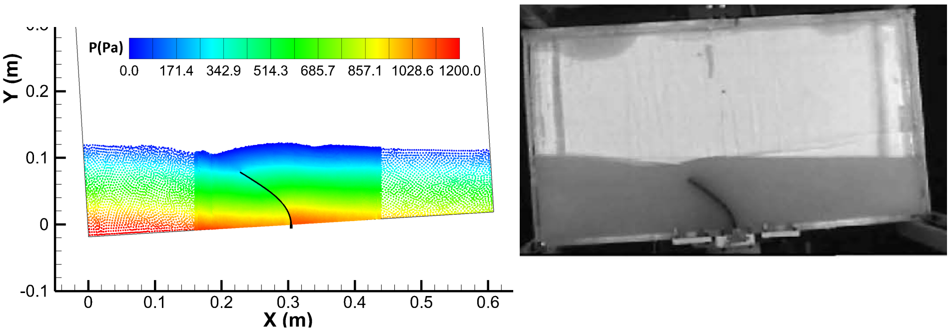

t = *2.12 s*

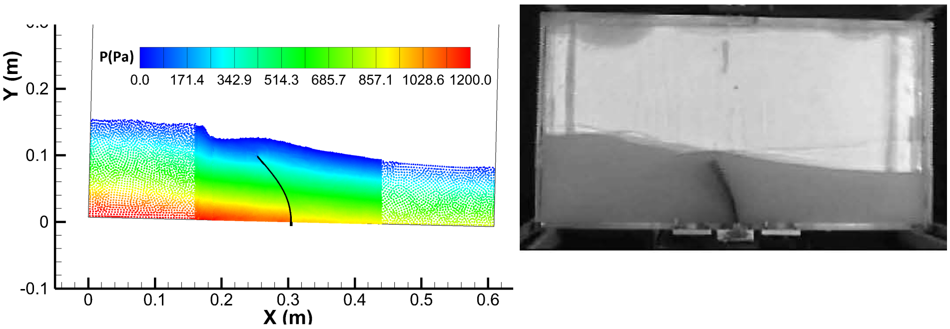

t = *2.32 s*

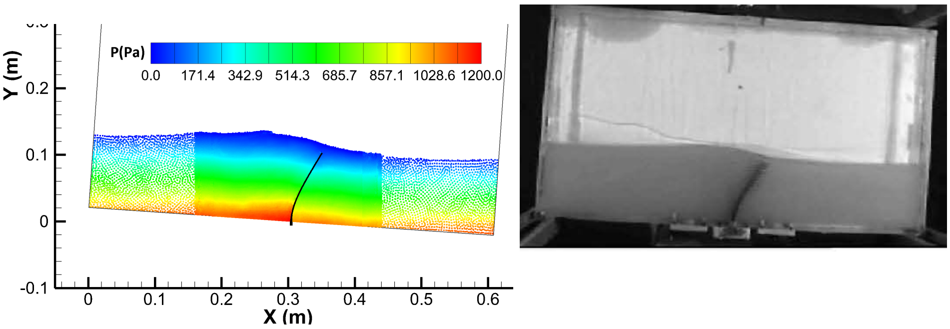

t = *2.56 s*

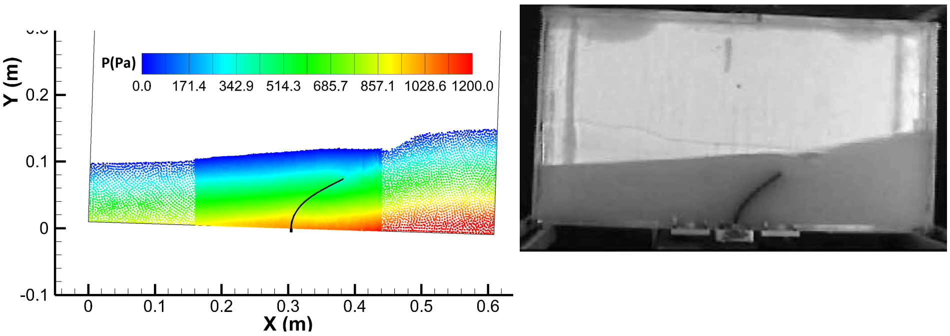

Figure 17. Sloshing tank interactions with an elastic beam in mid-depth oil: current simulation results (left) compared to the experiments [9] (right) at different instants (rows).

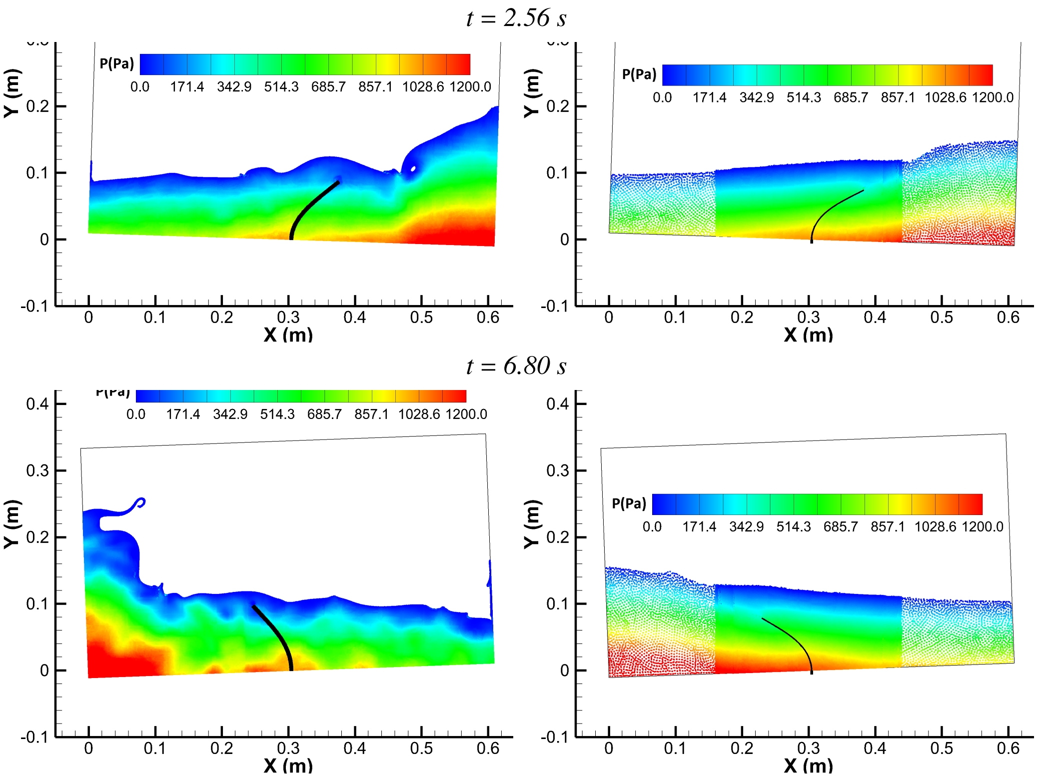

Figure 18. Sloshing tank interactions with an elastic beam in mid-depth oil: pressure field comparisons for 2D (left) and 3D (right) simulations at different instants.

4.2.2. *Clamped beam in shallow oil configuration*

A 57.4 mm oil depth is considered here. 2D numerical results can be found in Degroote *et al.* [20] and Paik & Carrica [59]. Three refinement levels are considered here according to the configuration displayed in Fig. 19, with Δx_{SPH} = 4 mm in the coarsest zone. All simulation parameters are presented in Tab. 3.

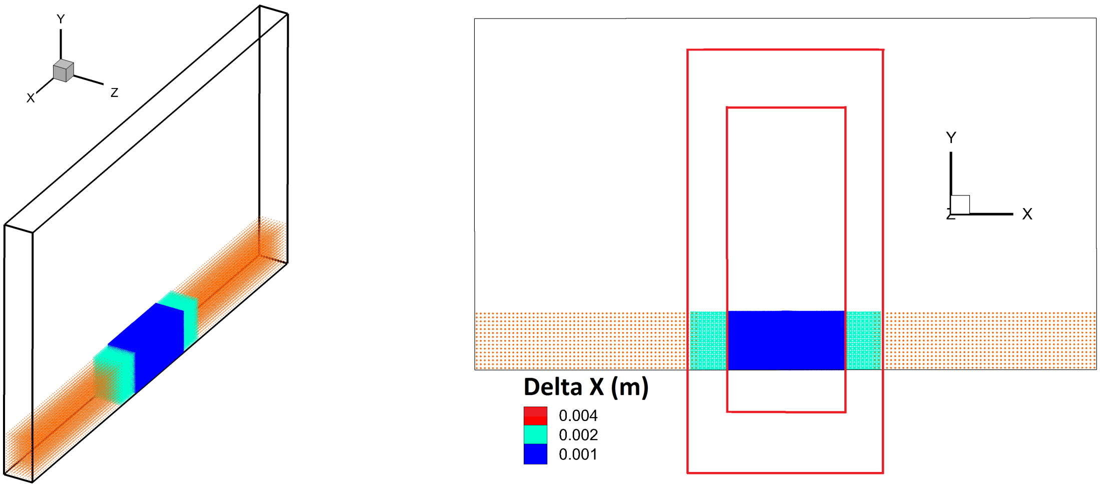

Figure 19. Sloshing tank interactions with a clamped beam in shallow oil with two refinement boxes (red) [9].

Tank dimensions	$L_x = 609\ mm$ $L_y = 334.5\ mm$ $L_z = 39\ mm$
Beam dimensions	$B_x = 4\ mm$ $B_y = 57.4\ mm$ $B_z = 33.2\ mm$
Oil depth	$57.4\ mm$
Poisson coefficient ν	≈ 0.5
Young Modulus	$6\ MPa$
ρ_{rubber}	$1100\ kg.m^{-3}$
ρ_{oil}	$917\ kg.m^{-3}$
ν_{oil}	$5.10{-}5\ m^2.s^{-1}$
g	$9.81\ m.s^{-2}$

Δx_{FE}	$0.5\ mm$
Δy_{FE}	$0.7175\ mm$
Δz_{FE}	$4.15\ mm$
Δx_{SPH}	$1\ mm$
$R/\Delta x_{SPH}$	2.11
C_0	$8.0\ m.s^{-1}$
CFL number	0.375

Table 3. Physical and numerical parameters for the sloshing tank interactions with an elastic beam in shallow oil.

The amplitude of the forced roll motion is also about 4 degrees (Fig. 20). This test case is more complex than the mid depth configuration since the beam deformations are smaller. In this configuration, the maximum beam deformation amplitude does not exceed 10 mm (see Fig. 21). The obtained numerical deformation is comparable to the experimental one both in phase and in amplitude. Nevertheless, the numerical results are farther from the experimental data than those obtained in the mid depth case (Fig. 16). These differences can be explained by some uncertainties in the experiments. According to Boita-Vera [9], the experiments did not seem to be completely repeatable and symmetric, especially for the shallow oil case. Besides, a more precise characterization of the rubber material would be needed to better represent its viscoelastic behaviour, which stands for an additional uncertainty. Note also that our 3D solution is in better agreement with the experiments that the 2D solution available in the literature. Here again, 2D simulation leads to a more dynamic flow.

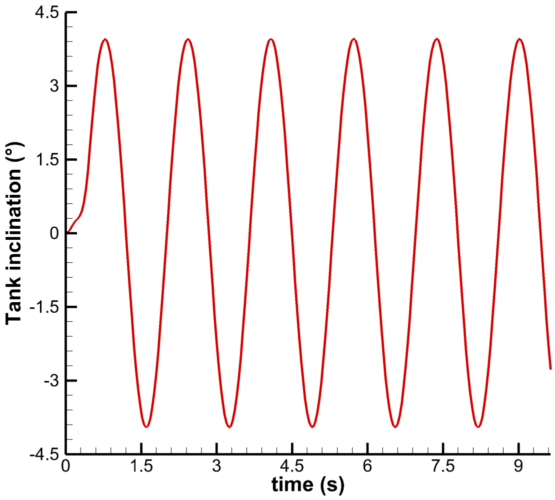

Figure 20. Time history of the tank inclination for the sloshing tank interactions with an elastic beam in shallow oil..

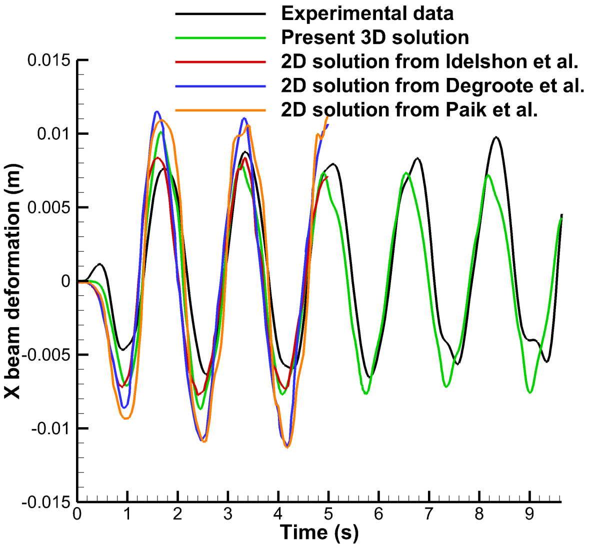

Figure 21. Time history of the local X-displacement of the beam extremity for the sloshing tank interactions with an elastic beam in shallow oil..

Here again, good agreements are observed between the numerical and the experimental free surface deformations (see Fig. 22).

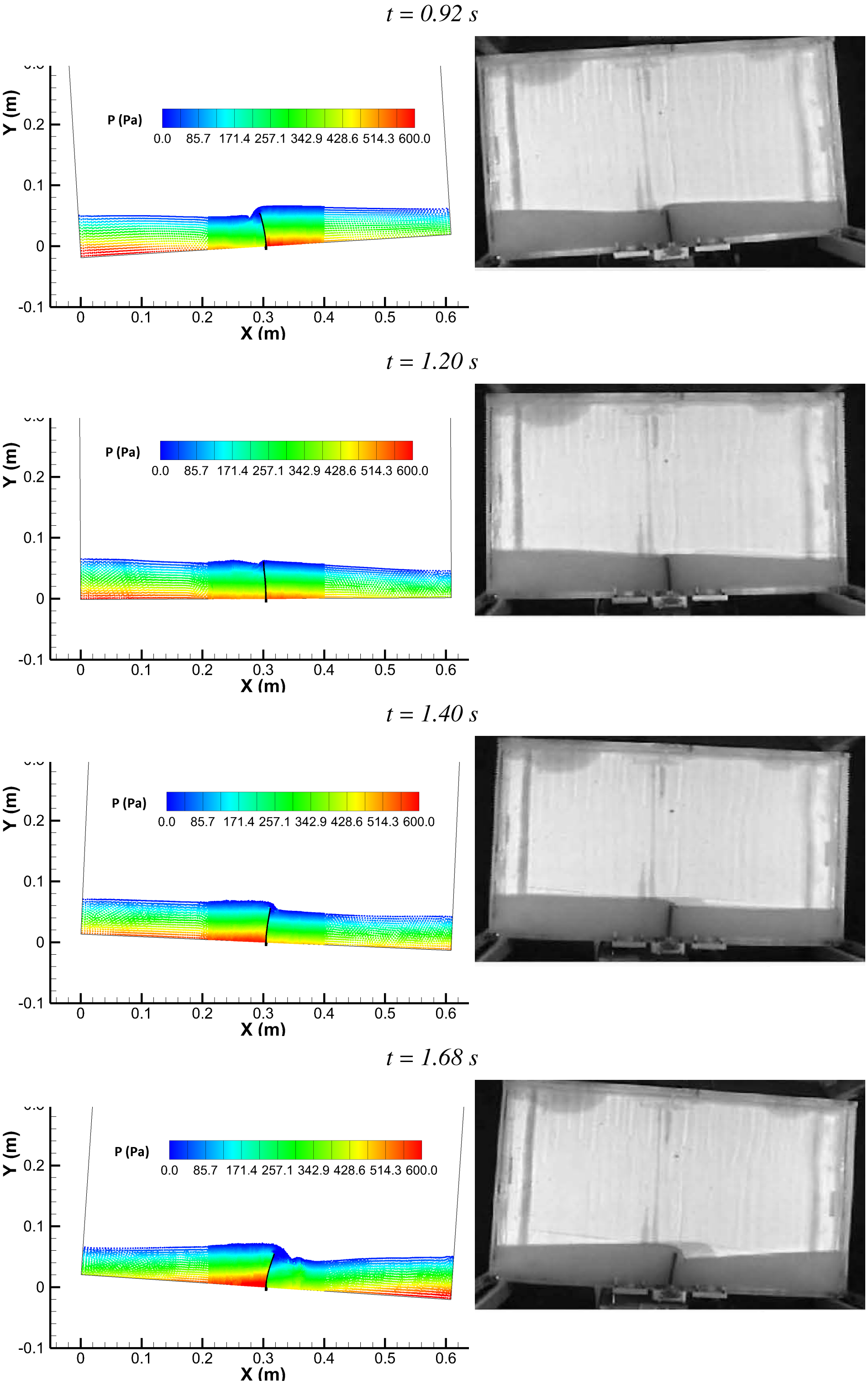
t = 0.92 *s*

t = 1.20 *s*

t = 1.40 *s*

t = 1.68 *s*

Figure 22. Sloshing tank interactions with an elastic beam in shallow oil: current simulation results (left) compared to the experiments [9] (right) at different instants (rows).

5. Tire model description

Simulations of a tire rolling through a puddle of water initially at rest (see Fig. 23) are proposed in this section. Classical hydroplaning simulations [15, 64, 39, 5] available in the literature considered smooth grounds. Nevertheless, the actual road is not smooth but conversely presents large irregularities. The main goal of this section is to quantify the road roughness influence on the tire grip performances. To this purpose, the model proposed consider a realistic rough road (see Fig. 24) so as to investigate the differences compared to a smooth ground configuration. The only difference lies in the rough nature of the road. These simulations aim at analysing how the fluid acts on this complex structure and how the tire deforms due to the presence of water. The possible persistence of a film of fluid entrapped between the tire and the road is also studied.

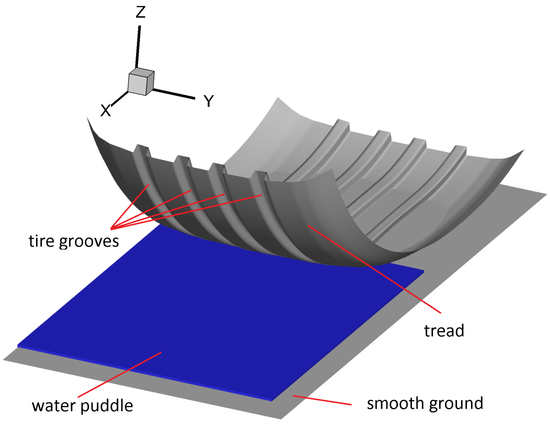

Figure 23. Hydroplaning configuration with perfectly smooth ground, the puddle initially at rest and the tire interface.

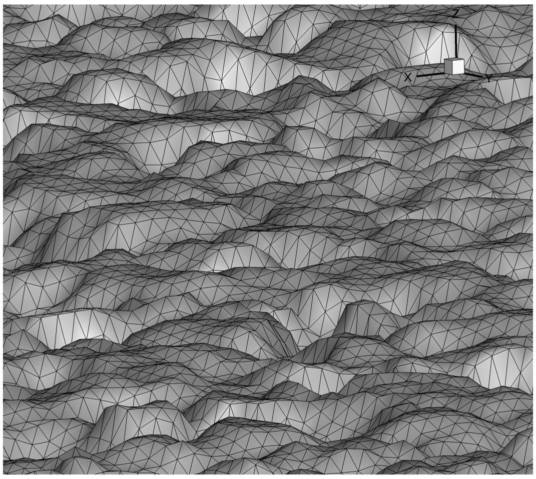

Figure 24. Rough road mesh.

In the literature, few works can be found concerning hydroplaning simulations on a rough ground. Besides, these studies are restricted to academic geometries, which are not representative of the reality, such as [3]. [43] proposed an hydroplaning simulation using a realistic rough ground, but in a demonstrative test case using a very simple tire model. The added value of the present work is to consider a realistic rough road with a complex tire description. The ground geometry used in the following simulations has been obtained from a real road measured at Michelin's proving ground similar to [70]. Indeed, it is possible to digitize the topography of a road thanks to imaging techniques. The ground is described by a (x,y) spatial resolution of 0.75 mm (see Fig. 24). With such a low resolution, only the macro-roughness are described.

The goal here is to get an idea of additional phenomena related to the combined presence of water and roughnesses. One can think for example of a fluid confinement inside the roughnesses of the ground so that the fluid gets pressurized, leading to the lift generation. It also comes to mind drainage mechanisms and notion of water depth; because imposing 1 mm height of water on a smooth ground is relatively different to 1 mm on a rough road where the definition of height is not unique. Here the water height is imposed at 1 mm above the top of the highest roughness. As it will be seen later, these issues need to be carefully studied. This water height is used during regulatory wet braking test of the European regulation N2009/1222. Furthermore, according to Biesse *et al.* [8] the water height on wet road in rainy conditions is 99 % of the time inferior to 1.0 mm.

The puddle is 266 mm long, 180 mm wide and 1 mm high. As the wheel enters the puddle, the fluid in front of the tire is entrapped between the tread and the ground and gets pressurized, leading to the lift generation. The spatial resolution in the fluid has been set to $\Delta x_{SPH} = 0.25$ mm to correctly capture the pressure field in this area while maintaining reasonable computational costs. The fluid domain is thus discretized with 5.6 and 3.1 million particles for the rough and the smooth ground configurations respectively, corresponding to thirty particles per groove width (see Fig. 23). The ratio $\frac{R}{\Delta x_{SPH}}$ has been set to 3.0 to ensure a good compromise between accuracy and needed computational resources. The maximum velocity in the fluid is expected to be lower than 30 $m.s^{-1}$. Therefore, the sound speed is set to 300 $m.s^{-1}$ to minimize the computational costs while ensuring the weakly-compressible assumption. The fluid simulation parameters are summarized in Tab. 4. Note that the complexity of the tire geometry requires the use of the NFM method for the solid boundary conditions in the SPH solver.

Physical time	10 ms
Water puddle dimensions	266 x 180 x 1 mm
ρ_{water}	1000 $kg.m^{-3}$
C_0	300.0 $m.s^{-1}$

Δx_{SPH}	0.25 mm
$R/\Delta x_{SPH}$	3.0
CFL number	0.375

Table 4. Hydroplaning simulation parameters.

The tire is modelled using an axi-symmetric tread and carcass (see Fig. 25). Among other materials, this complex composite is made of rubber, requiring elastic and hyper-elastic models. The hyper-elastic model of Mooney-Rivlin is used here. The tread spatial resolution is set to $\Delta x_{FE} = 2$ mm to properly capture the local deformations of the tread induced by the fluid loading, especially in the area where the water is entrapped between the tire and the ground. Such a fine spatial resolution is also needed to correctly handle the solid-solid contact between the tire sculptures and the smooth ground. Furthermore, the tire tread is only represented on a sector of 70 degrees out of the 360 of the whole wheel, in order to limit the computational costs of the FE part (see Fig. 25).

The motion is imposed to the wheel center through horizontal and rotation velocities, corresponding to 80 $km.h^{-1}$ (maximal velocity of the regulatory wet braking test). Note that no friction is considered in all the following simulations. Furthermore, a HHT scheme is systematically used for the solid implicit time integration, with a damping value $\alpha_s = -0.3$.

The initialization of the solid part is performed through the following four steps:

1. Inflation at 0.2 MPa, static.
2. Vertical position setting in a first approximation with respect to the ground, static.
3. Vertical position setting by applying a load of 337 daN down to the wheel center, corresponding to the car weight on a single wheel, static.
4. Horizontal translation and rotation imposed to the rim flank. Note that no vehicle damper is considered here. The wheel is free to move in the vertical direction, dynamic.

6. Numerical results

The global characteristics of the hydroplaning simulations are detailed in the previous section. Here, preliminary numerical results are presented. Fig. 26 shows the complexity of the free surface at $t = 10$ ms (the tire interface is not represented for visibility purpose), outlining the complexity of the free surface deformations.

The computational costs are significant due to the complexity of the tire model and the fine fluid spatial resolutions needed in the puddle. Note that the FE solver requires larger CPU times to solve this complex problem than *SPH-flow* for a single time step. Furthermore, very small time steps ($\Delta t \approx 10^{-6}$ s) are imposed by the CFL condition of the SPH method, increasing the global computational cost. As a result, the simulation was performed using different time steps in each sub-domain, using the CPS procedure combined with a ratio $p = 8$. Theoretically, the CPU time in the solid sub-domain (and therefore the total simulation time) is expected to be reduced from a factor 6.4 (Eq. (22)) provided that sufficient computing resources are allocated. Here, 120 cores and 16 cores are used respectively for the fluid and the solid sub-domains. In practice, a factor 3.2 has been obtained on the total simulation time. The simulation needed approximately 72 hours.

Fig. 27 presents the time history of the vertical fluid force applied to the tire, showing a larger fluid lift in the rough ground simulation. For the smooth ground the support zone is located in front of the tread, while for the rough ground downstream the water remains within the roughnesses (see Fig. 29). Small water volumes are entrapped between the road and the tread during the tire displacement (Fig. 29). These particles did not escape through the roughness geometry or inside the longitudinal grooves. Note that the fluid lift in these configurations represent a non-negligible part of the solid loading imposed to the tire (10% to 20% of 337 daN). These magnitudes could appear important for a new ribbed tire. Nevertheless, as illustrated by Todoroff *et al.* [62] new tire tire shows limited hydroplaning

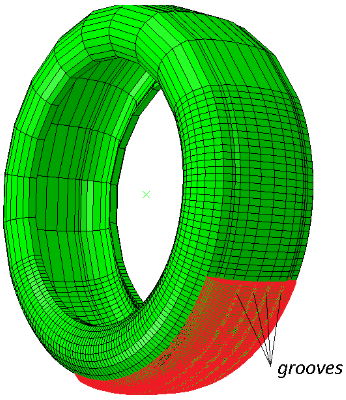

Figure 25. Tire tread (red) and carcass (green) used in the simulation.

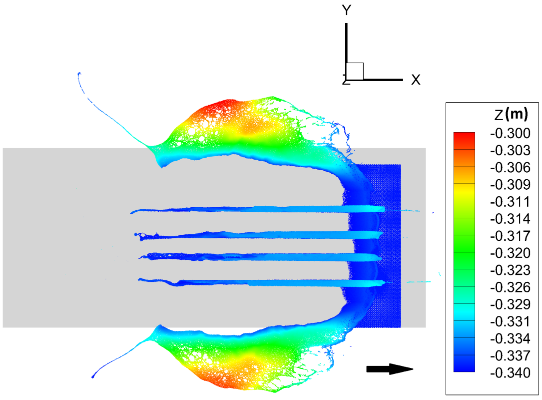

Figure 26. Free surface shape at t = 10 ms for the smooth ground configuration (the tire interface is not represented for visibility purpose).

mechanism for the speed encountered during the regulatory test. The wet braking test imposed by the European Legislation is performed from 80 km/h to 20 km/h. These hydrodynamics effects will only occur at the early stage of the braking test with limited influence on the final performance. Furthermore, there is no obvious link between the wet surface and the fluid lift, as the wet surface is monotonically increasing during the simulation (see Fig. 28).

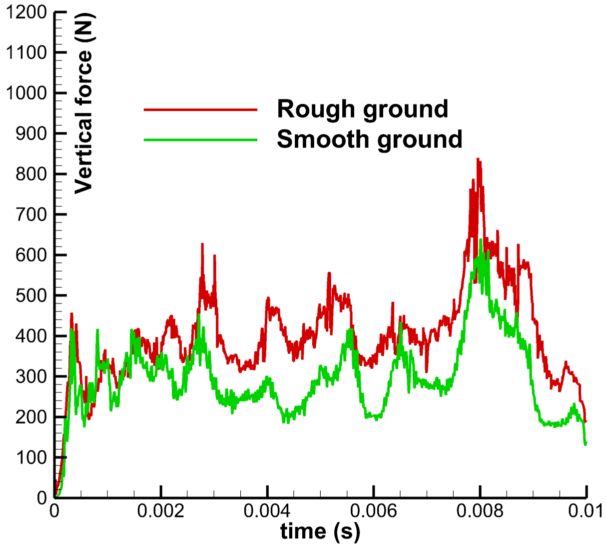

Figure 27. Time history of the vertical fluid force acting on the tire.

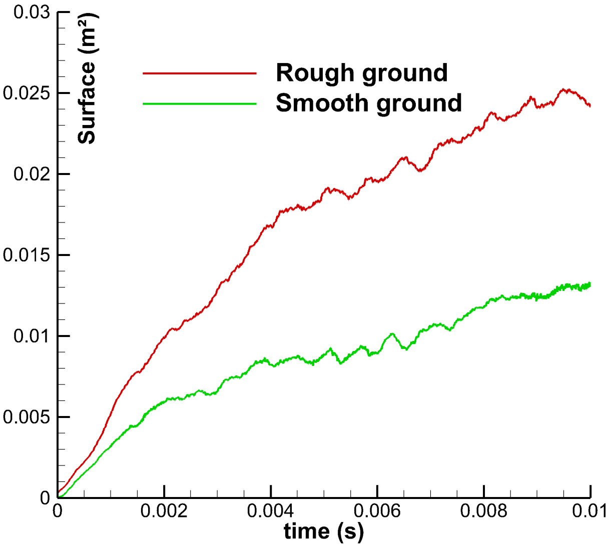

Figure 28. Time history of the tire total wet surface.

Fig. 29 displays some snapshots of the velocity field at different instants. Most of the water is drained to the front of the tread (see Fig. 30). We observe that the tire evacuates water particles with higher blasting velocities using the smooth road than the rough one, the volume of water is removed more quickly from the road. The second major portion is discharged into the longitudinal grooves. The highest velocities are observed in the jets formed at the beginning of the grooves from the water locally evacuated under the tire. Note that the grooves are more filled with water using the rough ground. Indeed the water height is imposed at 1 mm according to the maximal roughness. The fluid inside the roughnesses corresponds to an additional volume to evacuate compared to the smooth ground one.

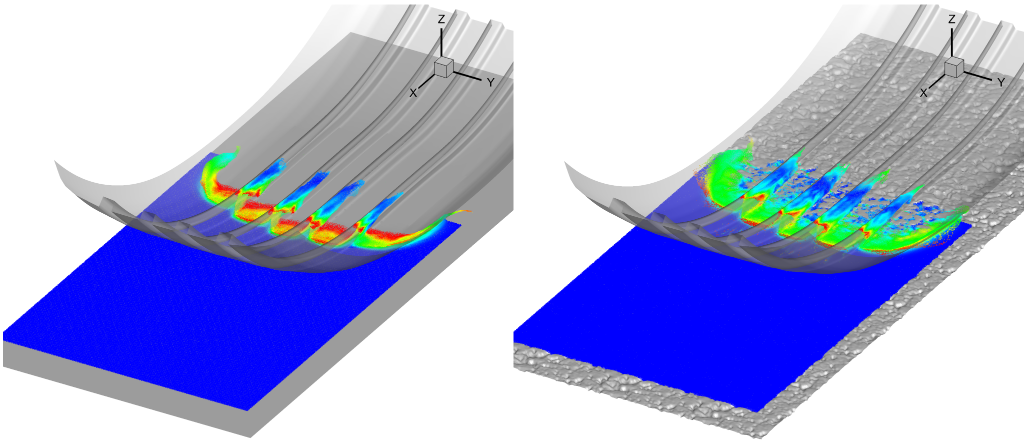

(a) t = 2.5 ms

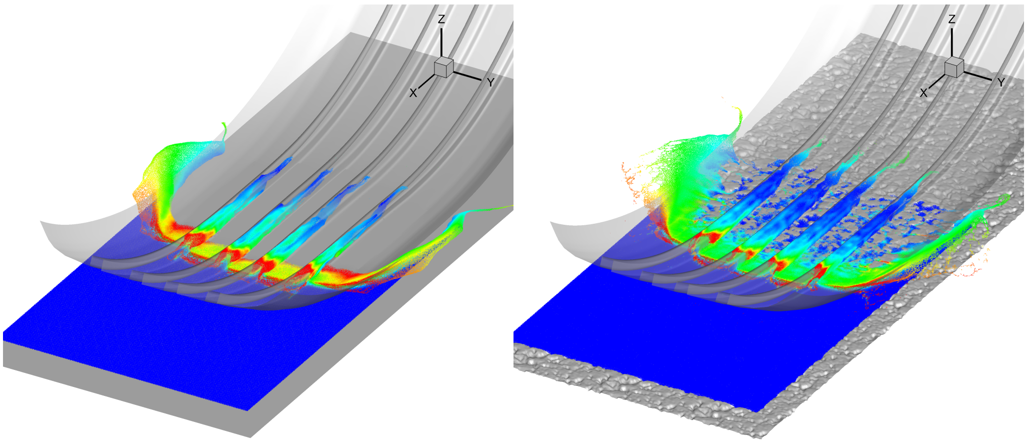

(b) t = 5.0 ms

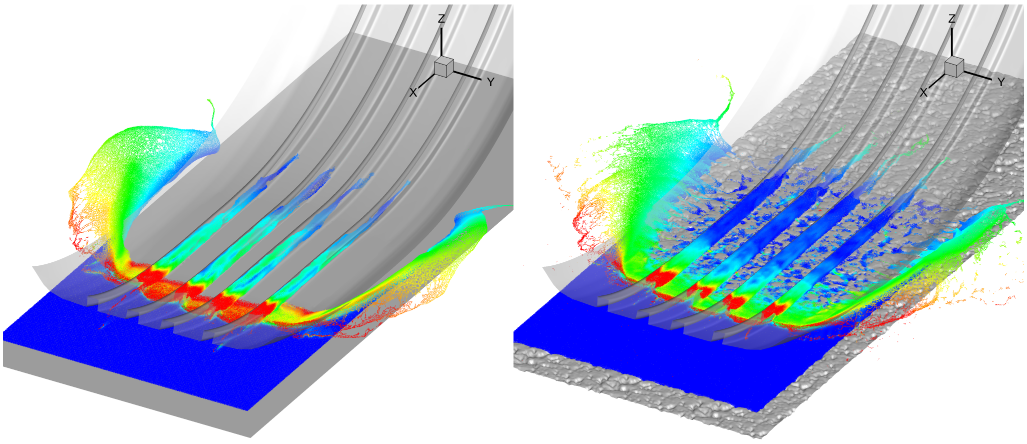

(c) t = 7.5 ms

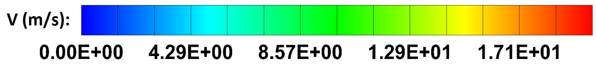

Figure 29. Velocity field at different instants using the smooth (left) and the rough (right) grounds.

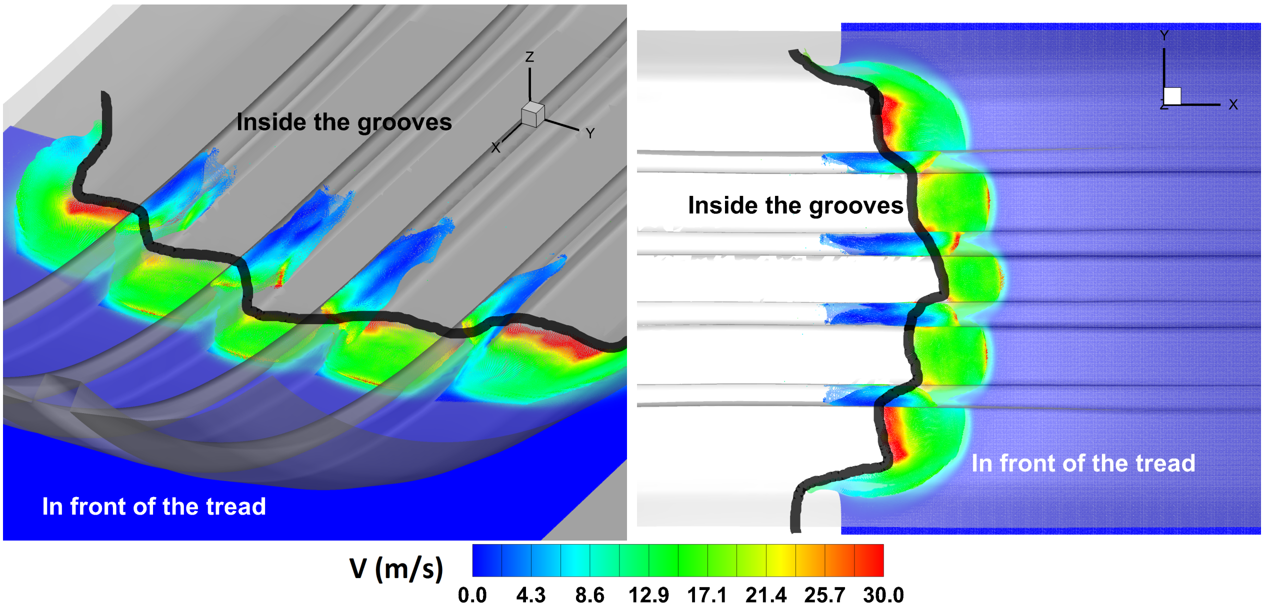

Figure 30. Zoom of the velocity field at t = 2 ms.

Looking carefully at the velocity field in the Fig. 30, the flow exceeds 30 $m.s^{-1}$ in some areas so that the Mach number is locally higher than 0.1. The validity of our weakly-compressible approach needs therefore to be checked to ensure the relevance of the FSI model. For that purpose, higher values of the sound speed have been tested, C_0 =600 and C_0 =1500 $m.s^{-1}$. For this parametric study, the physical durations have also been reduced to 5 and 2 ms respectively to limit the computational costs issues. Fig. 31 presents the time history of the resulting vertical fluid forces, showing very small differences for the different sound speed values. These results ensure both the validity of the weakly-compressible approach with C_0 = 300 $m.s^{-1}$ and the acceptable minimization of the number of SPH time steps thanks to this lower sound speed.

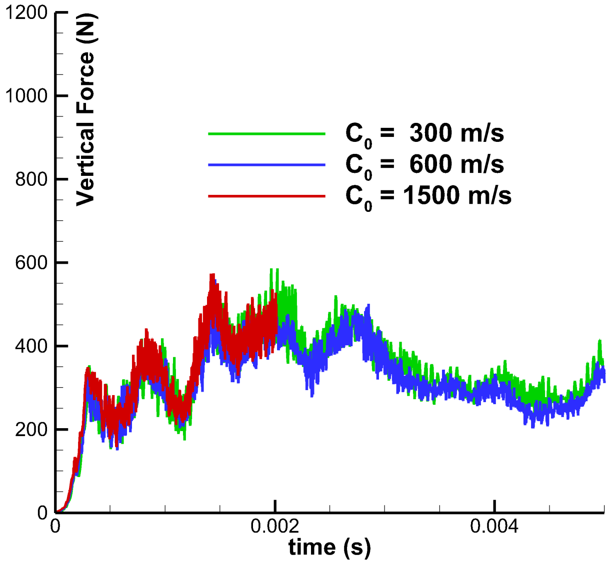

Figure 31. Time history of the vertical fluid force acting on the tire for different sound speed.

As visible in Fig. 32 which compares the reaction force on the tire with dry and wet grounds, the fluid is actually responsible for a loss of the ground reaction force which is a key parameter of the grip performances. Note the poor control on this reaction force in the dry ground case. Indeed, the model imposes a solid loading of 337 daN and recovers a ground reaction of order 480 daN at the end of the simulation without any fluid-structure interaction. The oscillations are also significant: approximatively 200 daN are observed between minimum and maximum values. These force variations are reflected also on the contact surface between the ground and the tire (see Fig. 33). This surface is obtained from the *Abaqus* solver. It corresponds to a summation of the areas where the tire cells intersect the ground cells, which explains the differences between rough and smooth grounds. Note that both force and surface increase in a non-physical manner.

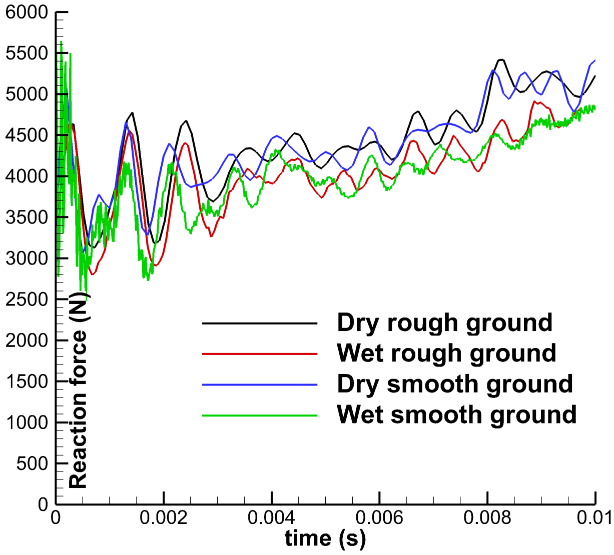

Figure 32. Time history of the vertical solid force on tire for wet and dry roads.

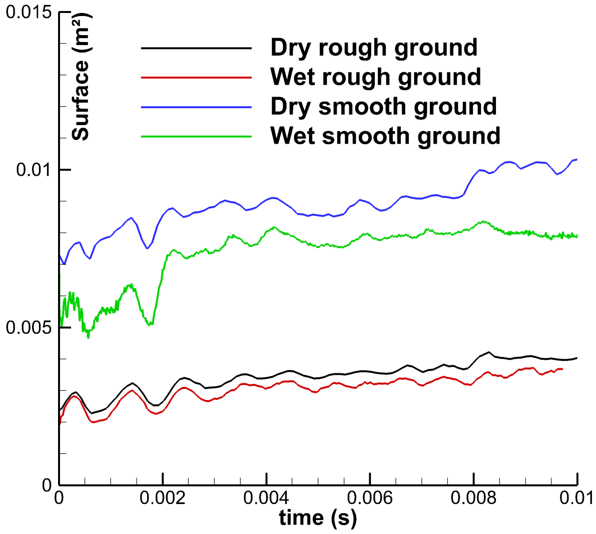

Figure 33. Time history of the solid-solid contact surface for wet and dry roads.

These differences could be explained by some difficulties in correctly representing the tire model using *Abaqus* software. Unfortunately, these uncertainties on the solid part prevent the validation of the FSI strategy with experimental data from Michelin's facilities. Indeed, the contact surface between the tread and the ground could be experimentally captured using imaging techniques, as shown in Fig. 34. For that purpose, the tire should be correctly modelled. Nevertheless, these uncertainties on the solid modelling do not prevent us from studying the performances of the present FSI coupling and the physic of aquaplaning problems in relative terms. As expected the contact surface is lower with the wet ground. The differences between wet and dry roads can be studied, and it is then possible to analyse (at least partially) the water effects on the global tire grip properties.

For example, the total wet surface can be separated into three parts: the wet area in front of the tread, the wet area inside the grooves and the wet area from the roughnesses (see Fig. 30). After $t = 5$ ms, the wet surface area in front of the tire tends to reach a steady state, as visible in Fig. 35 and Fig. 36. Conversely, no steady state is reached in the grooves yet. Water jets need longer times to propagate inside the tire structures. The simulation is extended to 10 ms in order to let the flow to fully develop, but this is still not sufficient. Nevertheless, it does not influence the fluid lift since the contribution of grooves is limited here to the fluid evacuation.

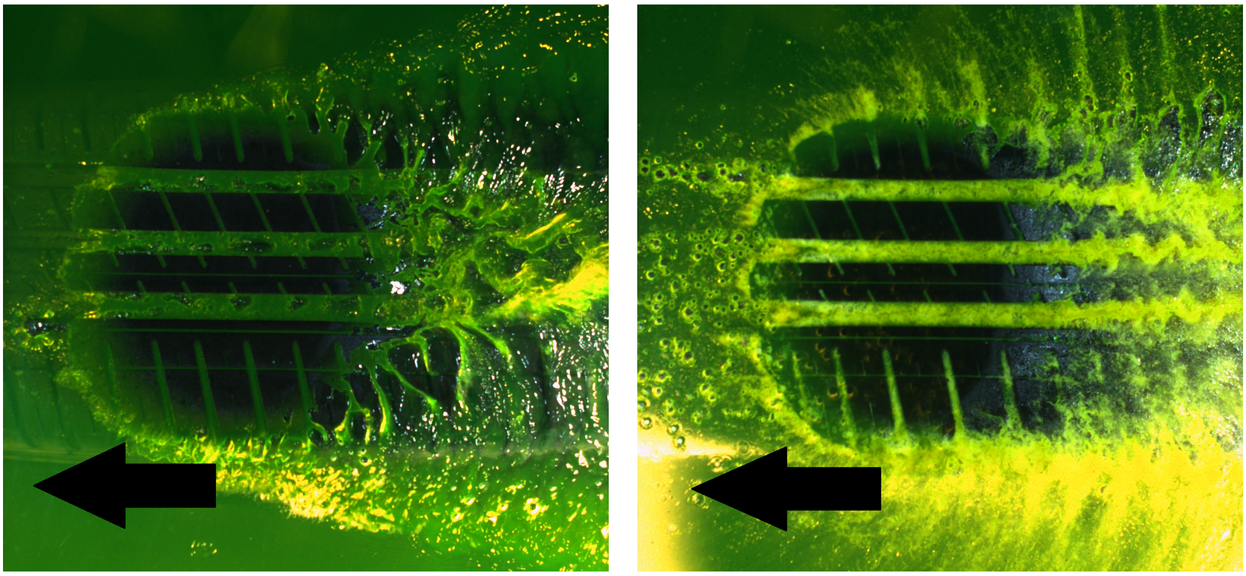

8 km.h^{-1}, water height: 1.5 mm *80 km.h^{-1}, water height: 1.5 mm*

Figure 34. Aquaplaning experimental tests.

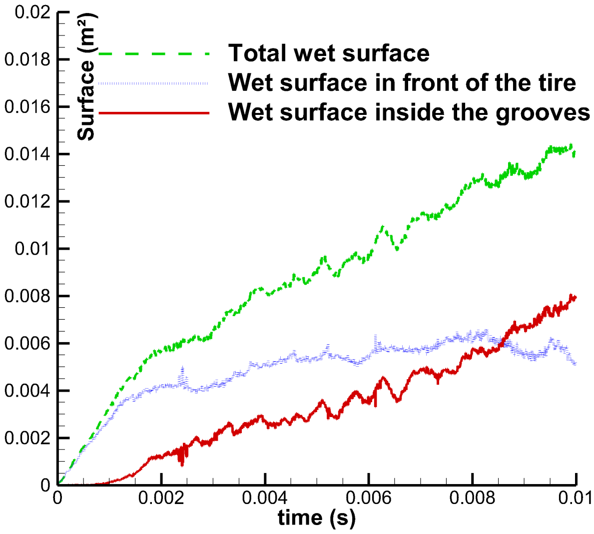

Figure 35. Time history of the tire wet surfaces, smooth ground configuration.

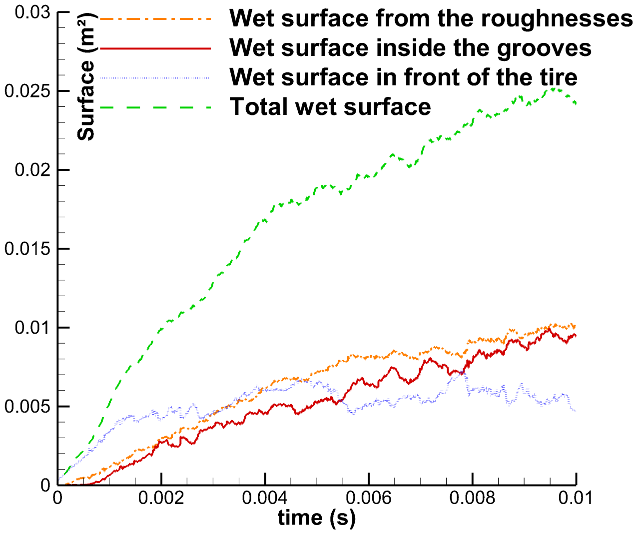

Figure 36. Time history of the tire wet surfaces, rough ground configuration.

The SPH-FE coupling can complete local or global experimental quantities for tire design purpose. For example, the less the water is evacuated into the grooves, the more its moves towards the water bead in front of the contact area. The fluid is then intensely pressurised. As a result, the tire is locally deformed by these strong fluid stresses. We propose here to study the local deformations at three rib cross-sections (of 4 mm width), as described in Fig. 37. Fig. 38 presents the results at $t = 2.5$ ms. The puddle of water tends to locally press the front of the tire. The deformations are larger in the lateral cross-sections than in the central one. Note also that the loss of contact surface is observed exclusively at the front (the back remains unchanged). Fig. 39 displays some snapshots of the contact pressure field due to the ground on the tire. Pressures have been limited to 3.10^5 Pa to make the observation easier and the tire moves from right to left. Looking carefully at these snapshots, the pressure distribution is only modified at the front (left side). Indeed, in this area the water tends to sustent the tire from the ground, reducing the contact pressure.

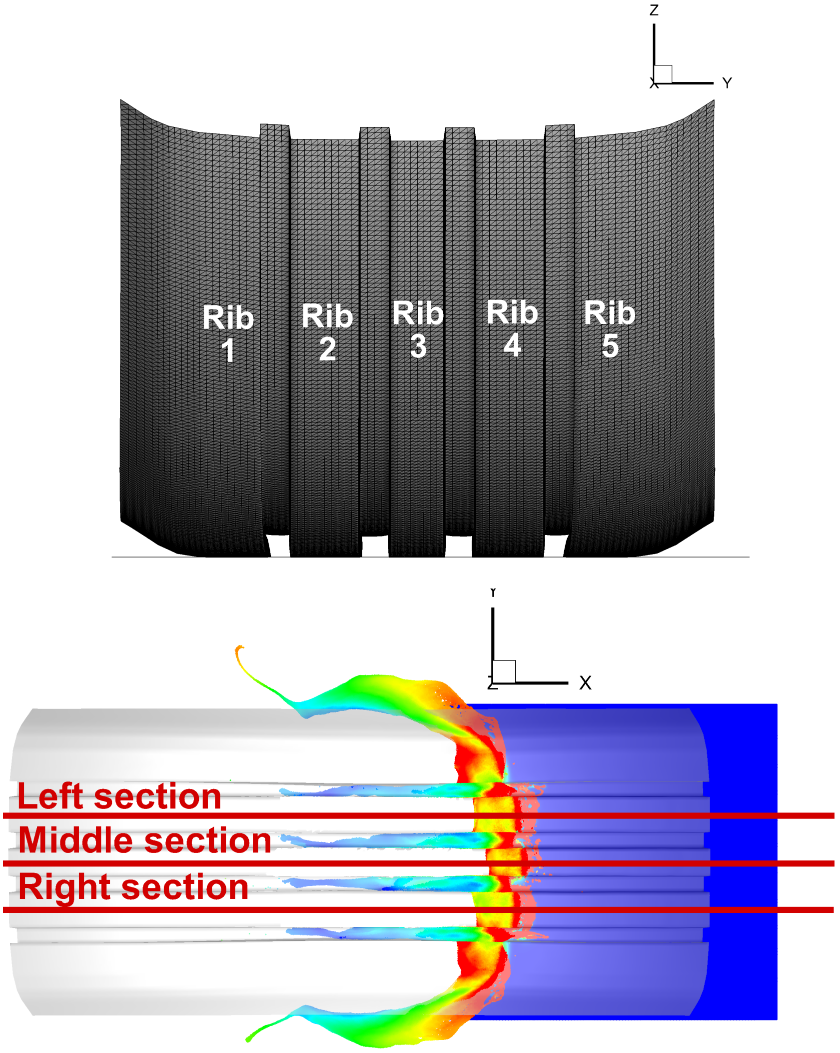

Figure 37. The rib cross-sections.

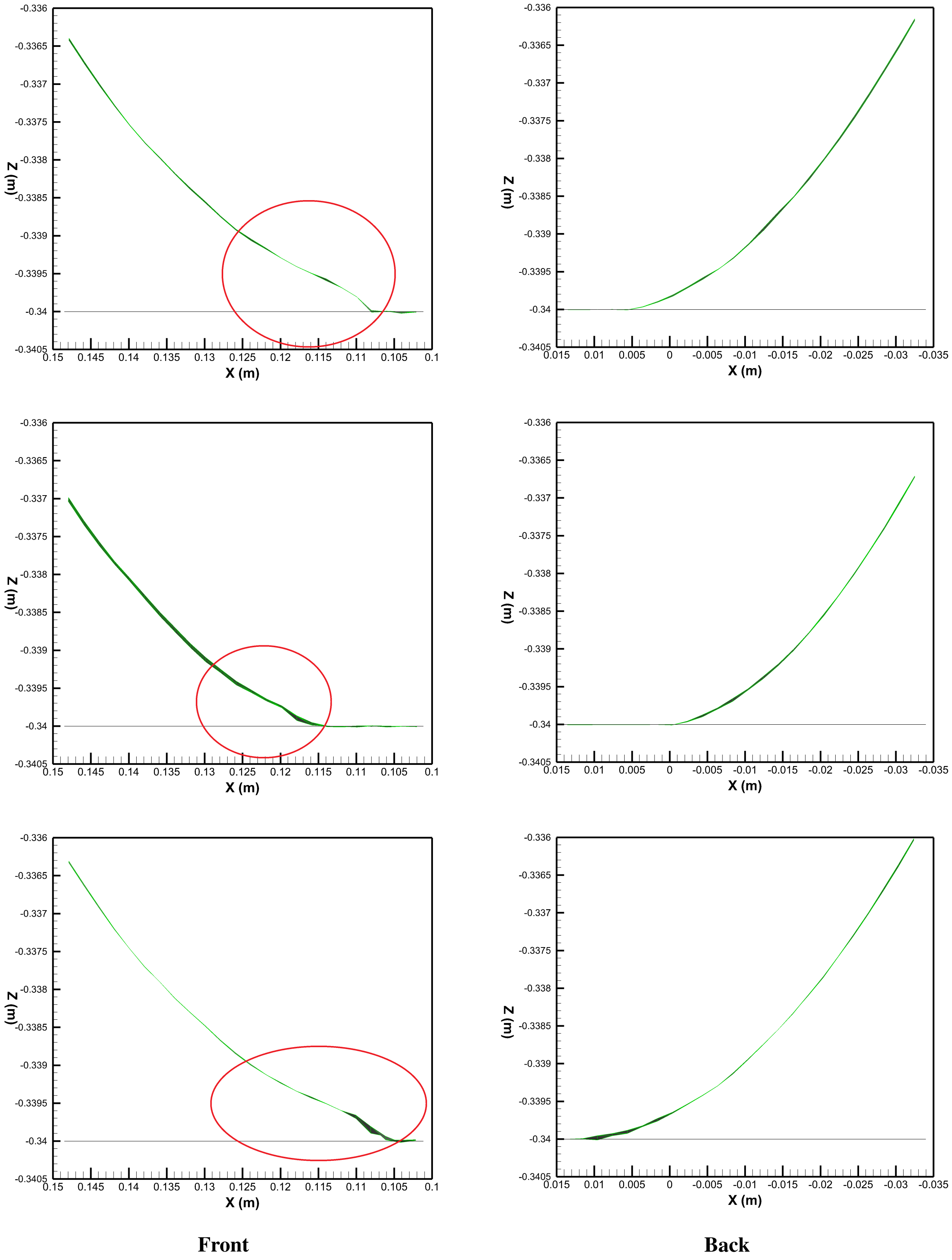

Figure 38. Tire profiles at the left (top), central (middle) and right (bottom) rib cross-sections at t = 2.5 ms, for a wet smooth road.

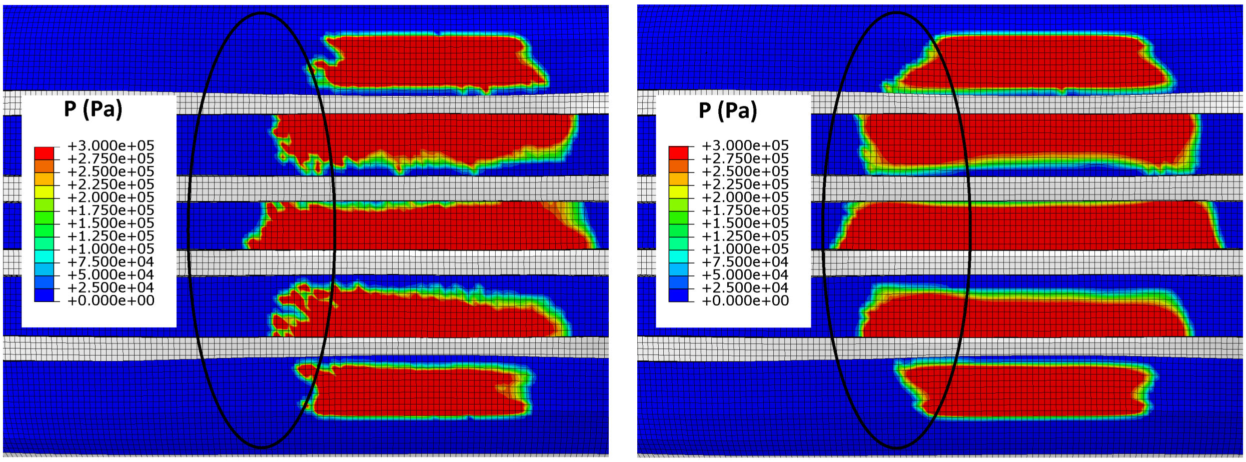

Wet ground *Dry ground*

Figure 39. Contact pressure field at $t = 2.5$ ms for wet and dry smooth roads.

This local elevation of the tire located in front of the contact area is responsible for a modification of the vertical displacement of the wheel center, as shown is Fig. 40. Note that the displacement on the dry road is already decreasing, due to the difficulties to properly model the tire structure in *Abaqus*. At $t = 10$ ms, the wheel center has moved of about 0.4 mm due to the fluid forces. This relative displacement remains small since a small water height is considered.

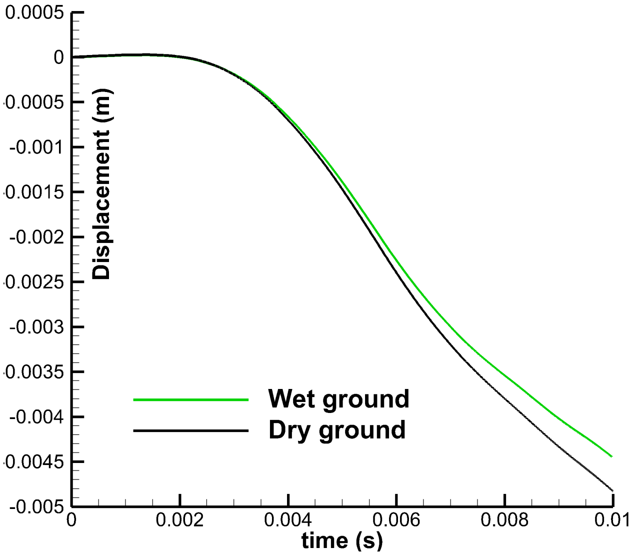

Figure 40. Time history of the wheel center vertical displacement for wet and dry smooth roads.

7. Conclusions

A 3D SPH-FE coupling for FSI problems has been proposed in this paper. An optimized cost-reducing algorithm dedicated to such SPH-FE coupling strategies has been proposed to improve the computational efficiency. A ratio between fluid and solid time steps has been introduced in order to minimize the computational cost by limiting the calls to the FE solver. Furthermore a control procedure based on the pressure loads has been proposed to preserve the accuracy and stability of the coupling. First of all, a validation of the FSI strategy has been investigated on various

3D test cases. Good agreements were obtained between experimental and numerical solutions. Then the feasibility of 3D hydroplaning simulations on rough ground using this SPH-FE coupling has been studied. The development of a complete tire model has been performed. This model is quite representative: pre-inflation, solid loading applied to the center of the wheel, initial contact setting, rotation and translation speeds imposed to the rim flank. The capability of the current FSI strategy to deal with this multi-dimensional problem involving complex interfaces has been demonstrated, helping in understanding the mechanisms at the origin of the hydroplaning effect. The present FSI strategy naturally considers the complex interfaces without any particular issue. These first simulations have provided coherent results to understand the rough ground influence for the hydroplaning phenomenon. In particular, it has been emphasized that the presence of road roughness is responsible for an increase of the fluid loading leading to a loss of contact between the tire and the ground. It has also been underlined that several parameters should be studied (fluid lift, wet surfaces, tire deformations, etc.). A whole wheel simulation with fine tire spatial resolution is presently unusable for computational time reasons. This is left for future work together with more thorough investigations of the phenomenon.

References

[1] C. ANTOCI. *Simulazione numerica dell'interazione fluido-struttura con la tecnica SPH*. PhD thesis, Ph.D thesis, Universit di Pavia, 2006.

[2] C. ANTOCI, M. GALLATI, and S. SIBILLA. Numérical simulation of fluid structure interaction by SPH. *IOP Computers and Structures*, 85(11–14):879–890, 2007.

[3] K. ANUPAM. *Numerical simulation of vehicle hydroplaning and skid resistance on grooved pavement*. PhD thesis, National University of Singapore, 2012.

[4] S.W. ATTAWAY, M.W. HEINSTEIN, and J.W. SWEGLE. Coupling of Smooth Particle Hydrodynamics with the Finite Element method. *Nuclear Engineering and Design*, 150:199–205, 1994.

[5] D. BARCAROLO, J. CANDELIER, D. GUIBERT, and M. DE LEFFE. Hydrodynamics performance simulations using SPH for automotive applications. *Proceedings of the 9th SPHERIC Conference*, 2014.

[6] D.A. BARCAROLO, G. OGER, and D. LE TOUZÉ. Adaptive particle refinement and derefinement applied to Smoothed Particle Hydrodynamics method. *Journal of Computational Physics*, 273:640–657, 2014.

[7] K.J. BATHE. Finite Element procedures. *Prentice Hall, 1st edition*, 1995.

[8] F. BIESSE. Analysis of wet road usage with a driving safety concern. *21st Technical Congress of the VDA*, 2019.

[9] E. BOTIA-VERA. *Experimental and statistical investigation of canonical problems in sloshing*. PhD thesis, Technical University of Madrid, 2015.

[10] B. BOUSCASSE, A. COLAGROSSI, S. MARRONE, and M. ANTUONO. Nonlinear water wave interaction with floating bodies in SPH. *Journal of Fluids ans Structures*, 42:112–129, 2013.

[11] F. CALEYRON, Y. CHUZEL-MARMOT, and A. COMBESCURE. Modeling of reinforced concrete trough SPH-FE coupling and its application to the simulation of a projectile's impact onto a slab. *International Journal for Numerical Methods in Biomedical Engineering*, 27:882–898, 2009.

[12] L. CHIRON. *Couplages et améliorations de la méthode SPH pour traiter des écoulements multi-échelles temporelles et spatiales*. PhD thesis, Ecole Centrale de Nantes, 2017.

[13] L. CHIRON, M. DE LEFFE, G. OGER, and D. LE TOUZÉ. Fast an accurate SPH modelling of 3d complex wall boundaries in viscous and non viscous flows. *Computer Physics Communications*, 234:93–111, 2019.

[14] L. CHIRON, G. OGER, M. DE LEFFE, and D. LE TOUZÉ. Analysis and improvements of adaptive particle refinement (APR) through CPU time, accuracy and robustness considerations. *Journal of Computational Physics*, 354:552–575, 2017.

[15] J.R. CHO, H.W. LEE, J.S. SOHN, G.J. KIM, and J.S. WOO. Numerical investigation of hydroplaning characteristics of three-dimensional patterned tire. *European Journal of Mechanics A/Solids*, 25:914–926, 2006.

[16] A. COLAGROSSI and A. LANDRINI. Numerical simulation of interfacial flows by smoothed particle hydrodynamics. *Journal of Computational Physcis, 191: 448-475*, 2003.

[17] M. DE LEFFE. *Modélisation d'écoulements visqueux par méthode SPH en vue d'application à l'hydrodynamique navale*. PhD thesis, Ph.D. Thesis, Ecole Centrale Nantes, 2009.

[18] T. DE VUYST. Coupling between meshless and Finite Element methods. *International Journal of Impact Engineering*, 31:1054–1064, 2005.

[19] J. DEGROOTE, P. BRUGGEMAN, R. HAELTERMAN, and J. VIERENDEELS. Stability of a coupling technique for partitioned solvers in FSI applications. *Computers & Structures*, 86:2224–2234, 2008.

[20] J. DEGROOTE, A. SOUTO-IGLESIAS, W. VAN PAEPEGEM, S. ANNEREL, P BRUGGEMAN, and J. VIERENDEELS. Partitioned simulation of the interaction between an elastic structure and free surface flow. *Computer Methods in Applied Mechanics and Engineering*, 199:2085–2098, 2010.

[21] J.B. DEUFF. *Extrapolation au réel des mesures de pressions obtenues sur des cuves modèle réduit*. PhD thesis, Ecole Centrale de Nantes, 2007.

[22] M. EL GINDY and Z. El SAYEGH. Sensitivity analysis of truck tyre hydroplaning speed using FEA-SPH model. *International Journal of Vehicle Systems Modelling and Testing*, 12:143–161, 2017.

[23] C. FARHAT and M. LESOINNE. Two efficient staggered algorithms for the serial and parallel solution of three dimensional nonlinear transient aeroelastic problems. *Computer Methods in Applied Mechanics and Engineering*, 182:499–515, 2000.

[24] G. FOUREY. *Développement d'une méthode de couplage fluide structure SPH Eléments Finis en vue de son application á l'hydrodynamique navale*. PhD thesis, Ecole Centrale de Nantes, 2012.

[25] G. FOUREY, C. HERMANGE, G. OGER, and D. Le TOUZÉ. An efficient FSI coupling strategy between smoothed particle hydrodynamics and finite element methods. *Computer Physics Communications*, 2017.

[26] J. GILBERT. *Accelerating an SPH-FEM Solver using Heterogeneous Computing for use in Fluid-Structure Interaction Problems*. PhD thesis, Virginia Polytechnic Institute and State University, 2015.

[27] R.A. GINGOLD and J.J. MONAGHAN. Smoothed Particle Hydrodynamics: theory and application to non-spherical stars. *Monthly Notices of the Royal Astronomical Society*, 181:375–389, 1977.

[28] H. GOTOH and A. KHAYYER. On the state-of-the-art of particle methods for coastal and ocean engineering. *Coastal Engineering Journal*, 60(1):79–103, 2018.

[29] P. GROENENBOOM and B. CARTWRIGHT. Hydrodynamics and fluid-structure interaction by coupled SPH-FE method. *Journal of Hydraulic Research*, 48:61–73, 2010.

[30] H. GROGGER and M. WEISS. Calculation of the hydroplaning of a deformable smooth-shaped and longitudinally-grooved tire. *Tire Science and Technology*, 25:265–287, 1997.

[31] C. HERMANGE, G. OGER, and D. Le TOUZÉ. Energy considerations in the SPH method with deformable boundaries and application to FSI problems. *Journal of Computational Physics X*, 2019.

[32] S-C HWANG, A. KHAYYER, H. GOTOH, and J-C PARK. Development of a fully lagrangian MPS-based coupled method for simulation of fluid-structure interaction problems. *Journal of Fluids and Structures*, 2014.

[33] S.R. IDELSOHN, J. MARTI, A. SOUTO-IGLESIAS, and E. ONATE. Interaction between an elastic structure and free-surface flows: experimental versus numerical comparisons using the PFEM. *Computational Mechanics, 43: 125-132*, 2008.

[34] G. JOHNSON. Linking of lagrangian particle methods to standard finite element methods for high velocity impact computations. *Nuclear Engineering and Design*, 150:265–274, 1994.

[35] A. KHAYYER, H. GOTOH, H. FALAHATY, and Y. SHIMIZU. An enhanced isph-sph coupled method for simulation of incompressible fluid-elastic structure interactions. *Computer Physics Communications*, 232:139–164, 2018.

[36] A. KHAYYER, N. TSURUTA, Y. SHIMIZU, and H. GOTOH. Multi-resolution MPS for incompressible fluid-elastic structure interactions in ocean engineering. *Applied Ocean Research*, 82:397–414, 2019.

[37] T.W. KIM and H.Y. JEONG. Hydroplaning simulation for tires using FEM, FDM and an asymptotic method. *Journal of Mechanical Science and Technology*, 11(6):901–908, 2010.

[38] M. KOISHI, T. OKANO, L. OLOVSSON, H. SAITO, and M. MAKINO. Hydroplaning simulation using fluid-structure interaction in LS-DYNA. *LS-DYNA conference*, 2001.

[39] S. KUMAR, K. ANUPAM, T. SCARPAS, and C. KASBERGEN. Study of hydroplaning risk on rolling and sliding passenger car. *Procedia - Social and Behavioral Sciences*, 53:1020–1028, 2012.

[40] J. LEDUC, F. LEBOEUF, and M. LANCE. Improvement of multiphase model using preconditioned riemann solvers. *Proceeding of the 5th international SPHERIC workshop*, 2010.

[41] Z. LI. *Développement d'une méthode de simulation de couplage fluide structure à l'aide de la méthode SPH*. PhD thesis, Ecole Centrale Lyon, 2013.

[42] Z. LI, A. COMBESCURE, and F. LEBOEUF. Coupling of Finite Volume and Finite Element subdomains using different time integrators. *International Journal For Numerical Methods in Fluids*, 72:1286–1306, 2013.

[43] Z. LI, J. LEDUC, J. NUNEZ-RAMIREZ, A. COMBESCURE, and J-C. MARONGIU. A non-intrusive partitioned approach to couple smoothed particle hydrodynamics and finite element methods for transient fluid-structure interaction problems with large interface motion. *Computational Mechanics*, 55(4):697–718, 2015.

[44] L. LIBERSKY, A. PETSCHEK, T. CARNEY, J. HIPP, and F. ALLAHDADI. High Strain Lagrangian Hydrodynamics: A three-dimensional SPH code for dynamic material response. *Journal of Computational Physics*, 109:67–75, 1993.

[45] L.B. LUCY. A numerical approach to the testing of the fission hypothesis. *Astronomical Journal*, 82:1013–1024, 1977.

[46] J-C. MARONGIU, F. LEBOEUF, J. CARO, and A. PARKISON. Free surface flows simulations in Pelton turbines using an hybrid SPH-ALE method. *Journal of Hydraulic Research*, 48:40–49, 2010.

[47] J.C. MARONGIU. *Méthode numérique lagrangienne pour la simulation d'écoulements à surface libre. Application aux turbines Pelton*. PhD thesis, Ecole Centrale de Lyon, 2007.

[48] S. MARRONE, A. COLAGROSSI, A. ANTUONO, G. COLICCHIO, and G. GRAZIANI. An accurate SPH modeling of viscous flows around bodies at low and moderate Reynolds numbers. *Journal of Computational Physics*, 245:456–475, 2013.

[49] S. MARRONE, A. COLAGROSSI, A. ANTUONO, C. LUGNI, and M.P. TULIN. A 2D+t SPH model to study the breaking wave pattern generated by fast ships. *Journal of Fluids and Structures*, 27(8):1199–1215, 2011.

[50] C. MICHLER, S.J. HULSHOFF, E.H. VAN BRUMMELEN, and R. DE BORST. A monolithic approach to fluid-structure interaction. *Computers & Fluids*, 33:839–848, 2004.

[51] J.J. MONAGHAN and R.A. GINGOLD. Shock Simulation by the Particle Method SPH. *Journal of Computational Physics*, 52:374–389, 1983.

[52] Y. NAKAJIMA, E. SETA, T. KAMEGAWA, and H. OGAWA. Hydroplaning analysis by FEM and FVM - effect of tire rolling and tire pattern on hydroplaning. *International Journal Automotive Technology*, 1 (1):26–34, 2000.

[53] J. NUNEZ RAMIREZ, J-C. MARONGIU, M. BRUN, and A. COMBESCURE. A partitioned approach for the coupling of SPH and FE methods for transient nonlinear FSI problems with incompatible time-steps. *International Journal For Numerical Methods in Engineering*, 109:1391–1417, 2016.

[54] G. OGER, M. DORING, B. ALESSANDRINI, and P. FERRANT. An improved SPH method: Towards higher order convergence. *Journal of Computational Physics*, 225:1472–1492, 2007.

[55] G. OGER, D. LE TOUZÉ, D. GUIBERT, M. DE LEFFE, J. BIDDISCOMBE, J. SOUMAGNE, and J.-G. PICCINALI. On distributed memory MPI-based parallelization of SPH codes in massive HPC context. *Computer Physics Communications*, 200:1–14, 2016.

[56] G. OGER, D. MARRONE, D. LE TOUZÉ, and M. DE LEFFE. SPH accuracy improvement through the combination of a quasi-Lagrangian shifting transport velocity and consistent ALE formalisms. *Journal of Computational Physics*, 313:76–98, 2016.

[57] C.W. OH, T.W. KIM, H.Y. JEONG, K.S. PARK, and S.N. KIM. Hydroplaning simulation for a straight-grooved tire by using FDM, FEM and an asymptotic method. *Journal of Mechanical Science and Technology*, 22(1):34–40, 2008.

[58] T. OKANO and M. KOISHI. Hydroplaning simulation using msc.dytran. 2001.

[59] K.J. PAIK and P.M. CARRICA. Fluidstructure interaction for an elastic structure interacting with free surface in a rolling tank. *Ocean Engineering*, 84:201–212, 2014.

[60] Q. QU, T. LIU, P. LIU, and R. AGARWAL. Simulation of water spray generated by pneumatic aircraft tire on flooded runway. *Conference AIAA Aerospace Sciences Meeting*, 2018.

[61] N.J. QUINLAN, M. BASA, and M. LASTIWKA. Tuncation errors in mesh-free particle methods. *International Journal for Numerical Methods in Engineering*, 66:2064–2085, 2006.

[62] V. TODOROFF, S. PAUPY, F. BIESSE, and Y. LE CHENADEC. The mechanisms involved during the wet braking of new and worn tires. *Vehicle System Dynamics*, pages 1–20, 2018.

[63] J.P. VILA. On particle weighted methods and Smooth Particle Hydrodynamics. *Mathematical Models and Methods in Applied Science*, 9(2), 1999.

[64] S. VINCENT, A. SARTHOU, J.P. CALTAGIRONE, F. SONILHAC, P. FÉVRIER, C. MIGNOT, and G. PIANET. Augmented lagrangian and penalty methods for the simulation of two phase flows interacting with moving solids. application to hydroplaning flows interacting with real tire tread patterns. *Journal of Computational Physics*, 230:956–983, 2011.

[65] H. WENDLAND. Piecewise polynomial, positive definite and compactly supported radial function of minimal degree. *Advances in Computational Mathematics*, 4:389–396, 1995.

[66] Q. YANG. *SPH Simulation of Fluid Structure Interaction Problems with Application to Hovercraft*. PhD thesis, Faculty of the Virginia Polytechnic Institute and State University, 2012.

[67] Q. YANG, V. JONES, and L. MCCUE. Free-surface flow interactions with deformable structures using an SPH-FEM model. *Ocean Engineering*, 55:136–147, 2012.

[68] Y. ZHANG and W. DECHENG. MPS-FEM coupled method for sloshing flows in an elastic tank. *Ocean Engineering*, 152:416–427, 2018.

[69] Z. ZHANG, H. QIANG, and W. GAO. Coupling of Smoothed Particle Hydrodynamics and Finite Element method for impact dynamics simulation. *Engineering Structures*, 33:255–264, 2011.

[70] S. ZHU, X. LIU, Q. CAO, and X. HUANG. Numerical Study of Tire Hydroplaning Based on Power Spectrum of Asphalt Pavement and Kinetic Friction Coefficient. *Advances in Materials Science and Engineering*, 2017.